Marine and Petroleum Geology 143 (2022) 105805

Contents lists available at ScienceDirect

Marine and Petroleum Geology

journal homepage: www.elsevier.com/locate/marpetgeo

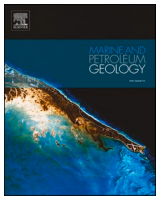

Fault analysis of a salt minibasin offshore Espírito Santo, SE Brazil: Implications for fluid flow, carbon and energy storage in regions dominated by salt tectonics

Qiang Zhang [a,*], Tiago M. Alves [a], Marco Antonio Caçador Martins-Ferreira [b]

[a] 3D Seismic Lab, School of Earth and Environmental Sciences, Cardiff University, Main Building, Park Place, Cardiff, CF10 3AT, United Kingdom
[b] Faculdade de Ciências e Tecnologia, Universidade Federal de Goiás, Conde Dos Arcos, 74968755, Aparecida de Goiânia, GO, Brazil

ARTICLE INFO

Keywords:
Listric faults
Hydrocarbon source rocks
Diapirism
Fluid migration
Salt minibasin
SE Brazil

ABSTRACT

High-quality 3D seismic reflection and well data are used to investigate the distribution, evolution history and significance of tectonic faulting in a salt minibasin offshore Espírito Santo, SE Brazil. Displacement-length (D_{max}-L) plots, displacement-depth (D-Z) plots and structural maps are compiled to understand the growth history of distinct fault families. Interpreted structures include crestal, corridor, listric and keystone faults. Their geometry, orientation and relative distribution reveal important differences. In detail, listric faults were formed in the investigated salt withdrawal basin following a NW to WNW strike, and show multiple bright spots and pockmarks around them. The strata into which listric faults sole out have similar seismic, lithological and petrophysical characters to known Cenomanian to Turonian source rocks, which comprise shales and marls with high gamma-ray values. Low-amplitude to transparent seismic facies further indicate the presence of ductile, highly likely organic-rich shales and marls. As a result, three evolutionary stages can be identified: a) Stage 1 is characterised by the formation of NW- or WNW-striking listric faults, keystone faults and the onset of reactive diapirism; b) Stages 2 and 3 record active diapirism due to a relative increase in sediment loading, documenting the formation of many crestal, corridor and keystone faults. Importantly, normalised leakage factor analyses reveal keystone faults to be the most favourable pathways to fluid migrating in the investigated salt minibasin. Conversely, listric faults are likely to form barriers and baffles to fluid in their lower parts.

1. Introduction

Salt minibasins are small basins, or depressions, surrounded by upwelling salt whose movement is dependent on the loading of synkinematic strata onto relatively thick evaporite successions (Jackson and Talbot, 1986; Jackson and Hudec, 2017). This forms a feedback loop between continuous sedimentation in salt minibasins and halokinesis. Primary and secondary minibasins are two fundamental types of basin identified in such settings, resting either on autochthonous or allochthonous salt, or on an equivalent salt weld. Consequently, secondary minibasins do not contain the oldest suprasalt stratigraphy that marks the early stages of halokinesis (Pilcher et al., 2011; Jackson and Hudec, 2017). Distinct fault families may occur around salt minibasins, with their geometry, orientation and distribution being closely related to the growth of the minibasin per se (Lopez, 1990; Rowan et al., 1999). For example, crestal faults are commonly developed above salt structures that surround minibasins, and they usually form planar growth faults rooting into the crests of diapirs, generating symmetric grabens above the latter (Rowan et al., 1999; Van Den Berg et al., 2004). In parallel, corridor faults pertain to faults generated above buried salt pillows, observed to connect discrete, but distant, salt structures. Corridor faults are often planar and comprise structural corridors that are preferential pathways for fluid (Mattos and Alves, 2018). Listric faults are another geometry of faults commonly observed in salt minibasins (Lopez, 1990; Diegel et al., 1995; Rowan et al., 1999). Their dip becomes gentler with depth, a geometry resulting in their characteristic concave-upwards shape (e.g. Bally et al., 1981; Shelton, 1984; Imber et al., 2003). The generation of listric faults in salt minibasins is commonly associated with viscous or ductile layers at depth (Shelton, 1984; Dula Jr, 1991; Imber et al., 2003; Brun and Mauduit, 2008; Bose and Mitra, 2009) or, instead, overpressure build-up due to abnormal pore pressure gradients in faulted stratigraphic intervals (Mcneill et al.,

* Corresponding author.
E-mail address: zhangq63@cardiff.ac.uk (Q. Zhang).

https://doi.org/10.1016/j.marpetgeo.2022.105805
Received 14 July 2021; Received in revised form 7 June 2022; Accepted 13 June 2022
Available online 17 June 2022

1997; Mandl, 1999; Hillis, 2003; Suppe, 2014; Yuan et al., 2020). Sediment compaction also plays an important role in forming listric faults, as the faults must flatten after they are buried by continued sedimentation, due to sediment compaction (Davison, 1987; Cartwright and Lonergan, 1996; Cartwright and Mansfield, 1998; Xiao and Suppe, 1989). The development of these fault families, especially listric faults, in salt minibasins is significant for hydrocarbon exploration, fluid-flow characterisation and carbon and energy storage, as they can act as effective fluid pathways or, instead, can form favourable traps for fluid (Rowan et al., 1999; Cox et al., 2001; Gartrell et al., 2004).

As a typical salt-bearing basin in SE Brazil, the Espírito Santo Basin comprises multiple fault families developed in the vicinity of growing salt structures (Fiduk et al., 2004; Mattos and Alves, 2018). In this same basin, Demercian et al. (1993) and Fiduk et al. (2004) have related the largest listric faults to extension accomodated on the proximal parts of the margin due to gravitational spreading and gliding of overburden rocks over Aptian salt. Ze and Alves (2016) have shown that relatively small listric faults accommodate strain and stress on the crests of the salt structures. Ze and Alves (2021) have revealed the existence of fluid flow through strata-bound domino faults in vicinity of the study area, whereas Mattos and Alves (2018) have studied the fault families around salt diapirs, showing that fault corridors linking adjacent salt structures are favourable fluid migration pathways. Nevertheless, little is known about the distribution and evolution history of different fault families in large areas of SE Brazil, and the South Atlantic as a whole.

The aim of this paper is to investigate the distribution, evolution history and significance of distinct fault families in a salt minibasin formed in deep-water sectors of the Espírito Santo Basin (Fig. 3). This work will also implement stress analyses to the interpreted fault families in the study area and indicate the potential fluid flow pathways in salt minibasins. In summary, this paper addresses the following research questions:

a) What is the importance of listric faults and their soling out intervals as structures signing the presence of rheologically weak, muddy successions in salt minibasins?
b) What is the chronology of faulting around salt structures when comparing them to other fault families in the Espírito Santo Basin?
c) Which of the interpreted fault families is more favourable to form fluid-flow pathways in salt minibasins?

2. Geological setting

The Espírito Santo Basin is located on the southeast continental margin of Brazil and covers an area of ~125,000 km^2, of which 107,000 km^2 are located offshore (Fiduk et al., 2004; Gamboa et al., 2010) (Fig. 1). The basin is bounded to the north by the Abrolhos Plateau, a volcanic ridge separating the Espírito Santo Basin from the Mucuri and Cumuruxatiba basins. To the south, it is separated from the Campos Basin by a largely political boundary, as there is a continuum of rift, sub-salt and supra-salt units from the Campos to the Espírito Santo basins (Fiduk et al., 2004; Gamboa et al., 2010; Mattos and Alves, 2018). The Espírito Santo Basin includes a series of rift basins trending N–S to NNE-SSW that were formed due to Late Jurassic-Early Cretaceous continental rifting and subsequent breakup of the supercontinent Gondwana (Ojeda, 1982; Chang et al., 1992; Fiduk et al., 2004; Mohriak et al., 2008; Alves, 2012; Piedade and Alves, 2017). The tectonic evolution of the Espírito Santo Basin is similar to most rift basins in the South Atlantic Ocean, and can be divided into four separate stages: rift onset, syn-rift, transitional, and drift (Chang et al., 1992; Bruhn and Walker, 1997; Cobbold et al., 2001; Fiduk et al., 2004; Gamboa et al., 2012) (Fig. 2).

2.1. Rift-related evolution of the Espírito Santo Basin

The rift onset stage of the Espírito Santo Basin occurred in the Late

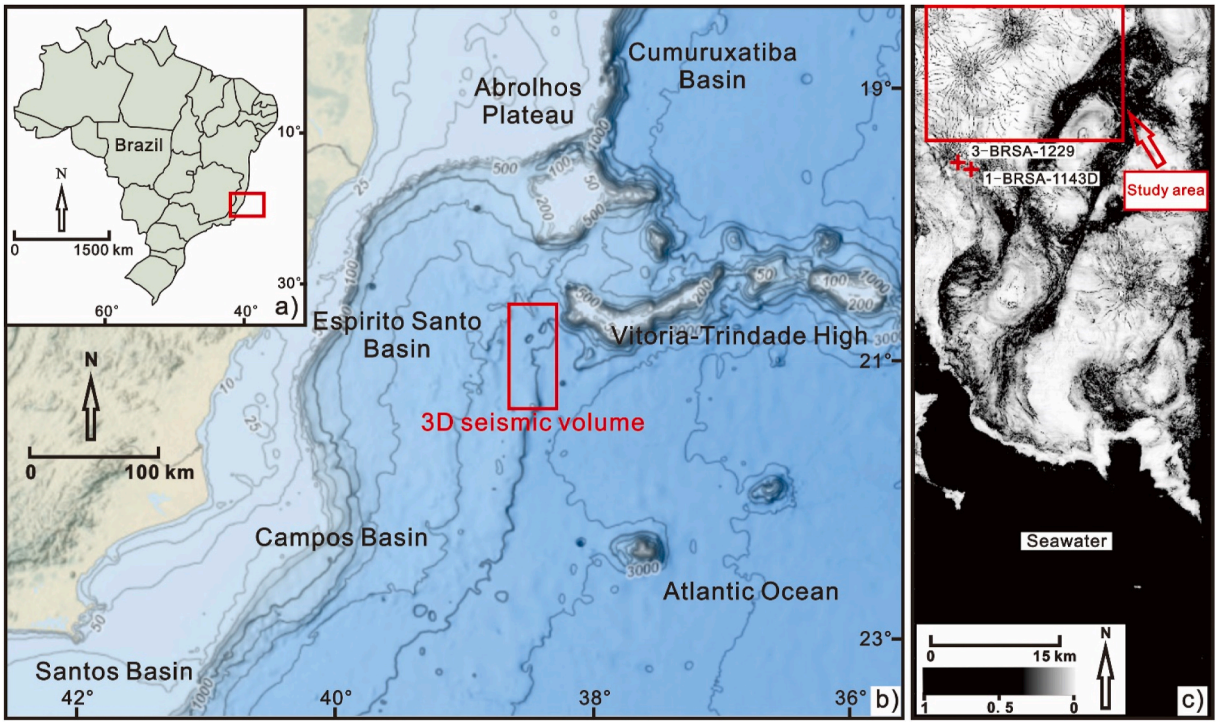

Fig. 1. a) Location of Fig. 1b) in relation to Brazil and its continental margin. b) Bathymetric map highlighting the location of the Espírito Santo Basin and its adjacent structural units. Note that the Espírito Santo Basin is bounded by the volcanic Abrolhos Plateau to the north, and it is separated to the Campos Basin to the south by a political boundary. The red polygon indicates the location of the 3D seismic volume. Topographic map is taken from the National Center for Environmental Information. c) Entire 3D seismic volume image showing the location of study area marked by a red polygon and two wells (3-BRSA-1229 and 1-BRSA-1143D) marked by red crosses in seismic variance time-slice (Z = −3000 ms two-way time). (For interpretation of the references to colour in this figure legend, the reader is referred to the Web version of this article.)

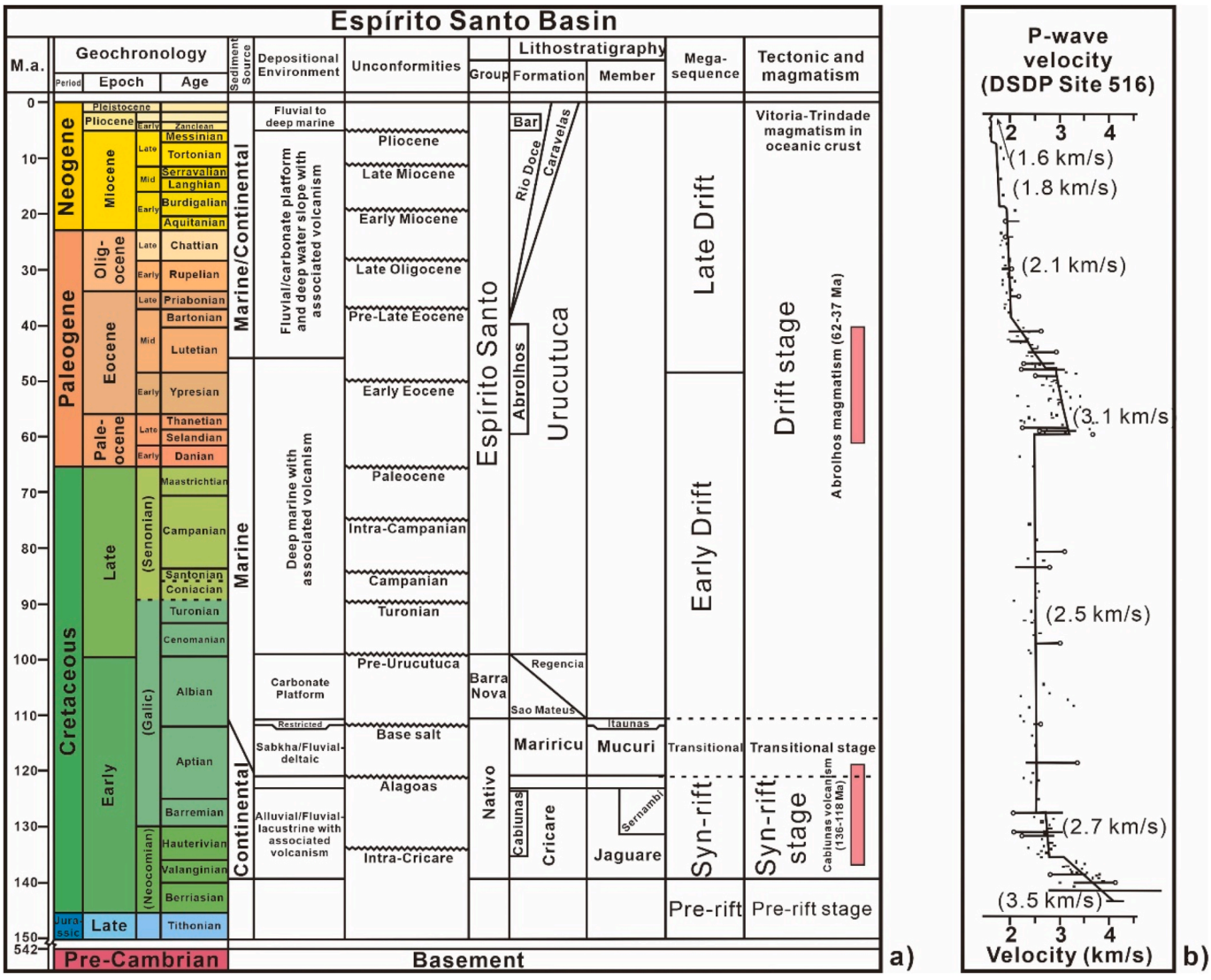

Fig. 2. a) Tectono-stratigraphic chart of the Espírito Santo Basin showing main depositional units and their depositional environments. Four tectonic evolutionary stages, episodes of magmatism and five megasequences are highlighted in the figure. Figure modified from Mattos and Alves (2018). b) Velocity data profile for well DSDP 516 for the Rio Grande Rise (Barker et al., 1983).

Jurassic-Early Cretaceous and was characterised by the initiation of lithospheric extension at a regional scale (Ojeda, 1982; Cainelli and Mohriak, 1999; Fiduk et al., 2004; Mohriak et al., 2008). Moderate tectonism and intense volcanism occurred throughout SE Brazil during this stage, with the Espírito Santo Basin becoming rapidly filled with coarse-grained fluvial sediment, alluvial fan deposits and localised evaporites (Ojeda, 1982; Chang et al., 1992; Cainelli and Mohriak, 1999; Mohriak and Rosendahl, 2003).

The syn-rift stage lasted from late Berriasian/Valanginian to the early Aptian (Ojeda, 1982; Fiduk et al., 2004; Gamboa, 2011; Qin et al., 2016). It was marked by intense tectonism due to the enhanced lithospheric extension and asthenospheric uplift that accompanied the formation of the Eastern Brazilian Rift (Cainelli and Mohriak, 1999; Mohriak and Rosendahl, 2003). Syn-rift units comprise lacustrine sediments in elongated and faulted sub-basins formed between the Santos and the Sergipe/Alagoas Basins. Three main facies associations were deposited at this stage: 1) alluvial fan/fan deltas and transitional deposits, 2) lacustrine marls and shales, and 3) lacustrine pelecypod limestones, usually termed *coquinas* (Ojeda, 1982; Demercian et al., 1993; Cainelli and Mohriak, 1999).

2.2. Halokinesis and Cenozoic evolution

The transitional stage occurred from early Aptian to late Aptian/early Albian, a period of time associated with continental breakup occurring to the east (i.e. outboard) of the Espírito Santo Basin (Ojeda, 1982; Fiduk et al., 2004; Alves et al., 2020). At this stage, the activity of large faults became concentrated at the locus of continental breakup to the east. Lithospheric extension significantly enhanced regional subsidence as recorded by the deposition of shallow water microbial carbonates, followed by the precipitation and accumulation of >3000 m of evaporites on the SE Brazil-West Africa conjugate margin (Davison et al., 2012). Such a transitional unit reflects a continental-breakup sequence with a typical regressive-transgressive cycle (Alves and Cunha, 2018; Alves et al., 2020).

The drift stage spanned from the Albian to present-day and marks the main phase of ocean spreading between South America and Africa (Ojeda, 1982; Fiduk et al., 2004; Gamboa, 2011). At this stage, tectonic activity was chiefly associated with thermal subsidence and marine deposition predominated in the Espírito Santo Basin (Chang et al., 1992; Cainelli and Mohriak, 1999). The drift stage comprises two distinct megasequences: an early drift transgressive megasequence and a late

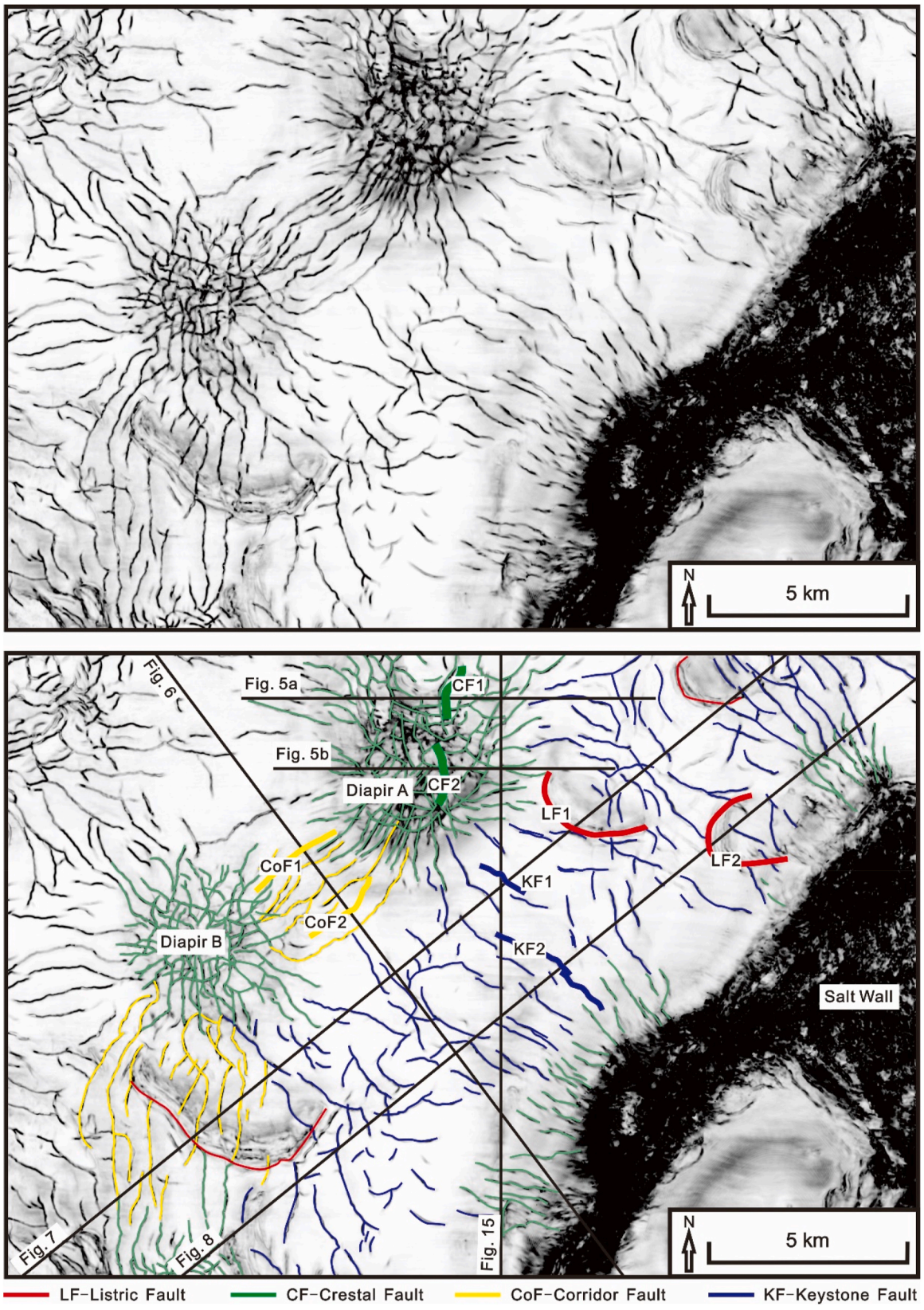

Fig. 3. Variance time-slice (Z = −3000 ms two-way time) of the study area highlighting the four fault families and salt structures interpreted in this work. Red, green, yellow, and blue lines indicate listric faults (LFs), crestal faults (CFs), corridor faults (CoFs) and keystone faults (KFs). The seismic profiles shown in Figs. 5–8 and 15 are shown by thin black lines. Eight representative faults from four fault families, shown with bold lines, were selected for our displacement-depth (D–Z) and displacement-length (D_{max}-L) analyses (see Figs. 11–14). (For interpretation of the references to colour in this figure legend, the reader is referred to the Web version of this article.)

drift regressive megasequence (Chang et al., 1992; Cainelli and Mohriak, 1999). The early drift transgressive megasequence records the deposition of carbonate intervals below muddy and sandy turbidites, representing shallow water environments that deepened upwards until the end of the Cretaceous (Ojeda, 1982; Chang et al., 1992; Mohriak et al., 2008; Qin et al., 2016). The late drift regressive megasequence was marked by open marine deposition, reflecting the progressive filling of the Espírito Santo Basin's continental shelf and slope (Ojeda, 1982; Chang et al., 1992; Mohriak et al., 2008).

Due to regional extension and continuous subsidence, halokinesis occurred in the study area in response to differential loading by overburden strata, gravity spreading and downslope gravity gliding on top of evaporite successions (Demercian et al., 1993; Fiduk et al., 2004). Halokinesis lasted from the Albian to Holocene but peaked during the Late Cenozoic (Fiduk et al., 2004; Alves, 2012). It divided the basin into three tectonic domains with different structural styles: proximal extensional, transitional and distal compressional (Rouby et al., 2003; Vendeville, 2005; Gamboa et al., 2010; Mohriak et al., 2012; Qin et al., 2016). The proximal extensional domain includes salt rollers, salt walls along conjugate normal faults, turtle anticlines and rafts (Mohriak et al., 2008). The transitional domain is characterised by salt diapirs, while the distal compressional domain is dominated by allochthonous salt (Demercian et al., 1993; Davison, 2007).

3. Data and methods

This paper uses a high-quality 3D seismic volume acquired in deepwater Espírito Santo Basin in 2004, covering 360 km^2 (Fig. 1). It was shot at a water depth ranging from 1630 to 2050 m. The seismic volume was acquired with a 6 × 5700 km array of streamers, and it was prestacked time migrated with a 12.5 × 12.5 m grid line spacing. Seismic data processing included resampling, spherical divergence corrections

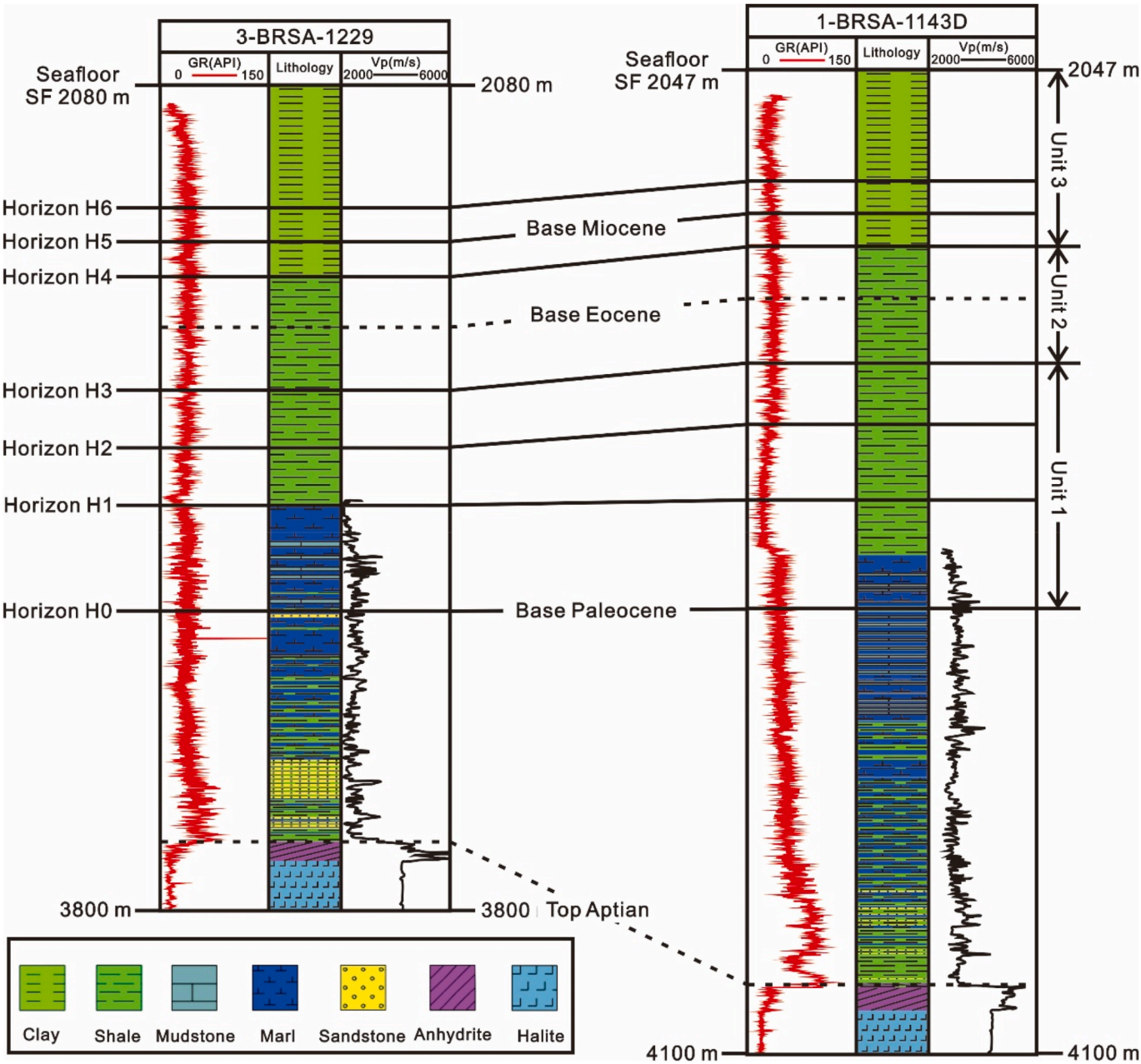

Fig. 4. Well profile correlation for Wells 3-BRSA-1229 and 1-BRSA-1143D located near the study area. Chronostratigraphic framework, lithology, gamma-ray (GR) and V_p (p-wave velocity) wireline curves are shown in the figure.

and zero-phase conversions, all undertaken prior to data stacking (Fiduk et al., 2004; Alves, 2012; Ze and Alves, 2016; Piedade and Alves, 2017). Data are displayed using the European SEG standard for polarity in which a change in acoustic impedance from low to high is shown as a red seismic reflection, and from high to low is shown in black. The seismic volume was processed in the time domain following a sampling rate of 2 ms, re-sampled at 4 ms, with a dominant frequency of 40 Hz. This resulted in a minimum vertical resolution (1/4 of the wavelet frequency, or $\lambda/4$) ranging from 11 to 19 m at the depth of strata investigated in this work (Mattos and Alves, 2018). In addition, two wells located in vicinity of the study area provide gamma-ray, lithology and V_p (p-wave velocity) data (Biancardi et al., 2020). Well correlations were also completed to identify lithological variations in the seismic-stratigraphic units interpreted in this study, and a chronostratigraphic framework was established based on Ze and Alves (2021) (Fig. 4).

The study area comprises a 20-km long, 6-km wide, NE-striking salt minibasin bounded to the west by two salt diapirs (A and B), and by a salt wall to the east (Figs. 1 and 3). Eight (8) key seismic-stratigraphic reflections, including the seafloor, were interpreted every ten lines (125 m) in our seismic volume (Figs. 5–8). Three principal stratigraphic units were defined based on their internal seismic reflection characters, bounding reflection terminations, and their relationship with main structural features. Variance time-slices were used to identify relevant fault families around salt structures (Fig. 3), as they clearly show important discontinuities on time slices, including faults and fractures (Brown, 2011).

Five hundred and thirty-four (534) faults were manually interpreted every two crosslines/inline (25 m). They were classified into four different fault families based on their geometry, orientation, distribution and relationship with main salt structures. This procedure guaranteed high-enough accuracy when recording displacement data for distinct fault segments, as it complies with the minimum sampling interval defined in Ze and Alves (2019). The latter authors proposed that minimum throw/displacement sampling intervals are related to the length of a fault; sampling intervals should be less than 5% of the fault length when the latter is < 3500 m, or 3% of the fault length when this is $>$

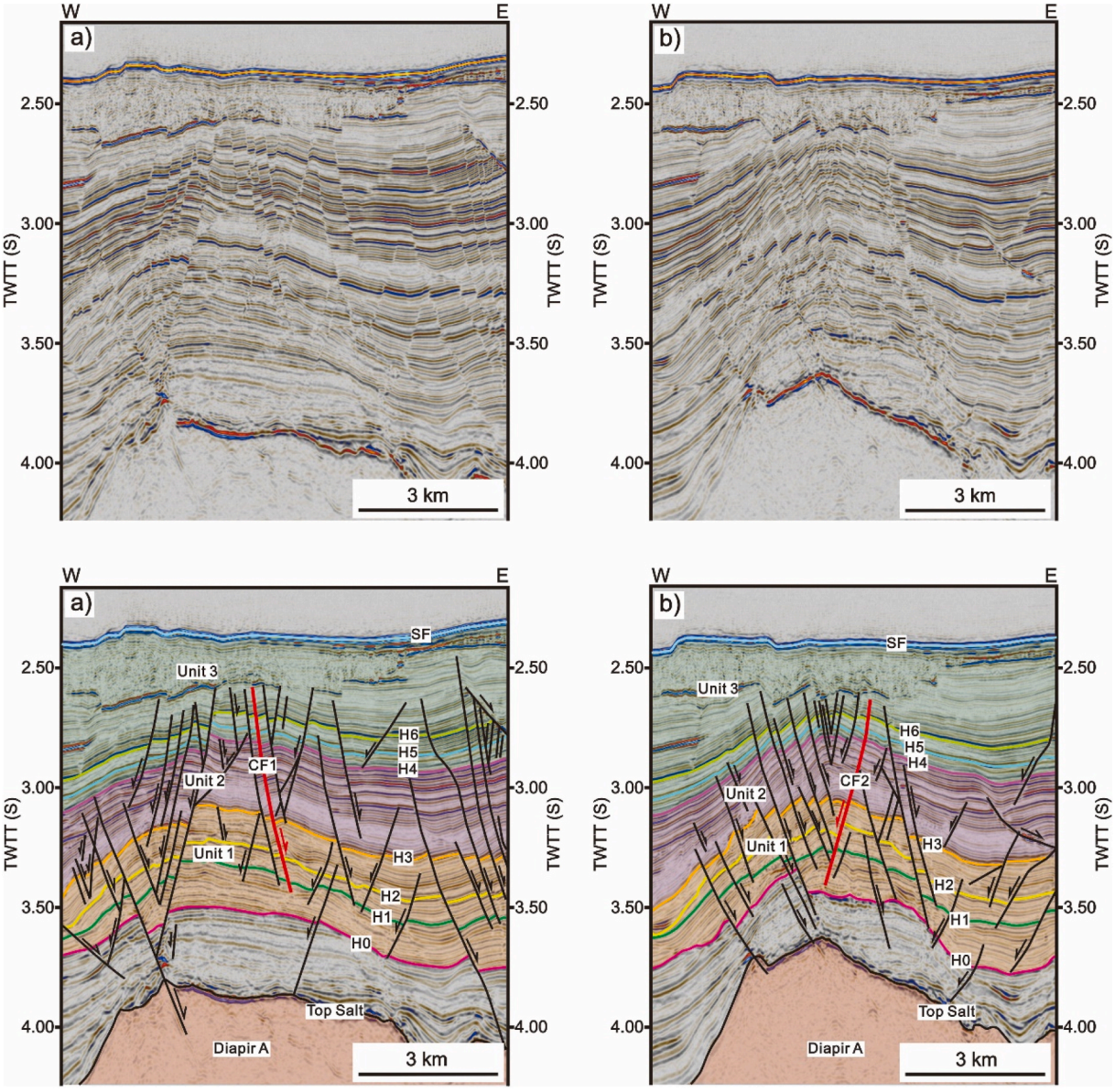

Fig. 5. Seismic profiles showing representative crestal faults 1 (CF1) and 2 (CF2) in the study area. Red bold and black lines represent faults, while other coloured lines mark the different seismic-stratigraphic horizons interpreted in the study area. The location of the seismic profile is shown in Fig. 3. SF=Seafloor. (For interpretation of the references to colour in this figure legend, the reader is referred to the Web version of this article.)

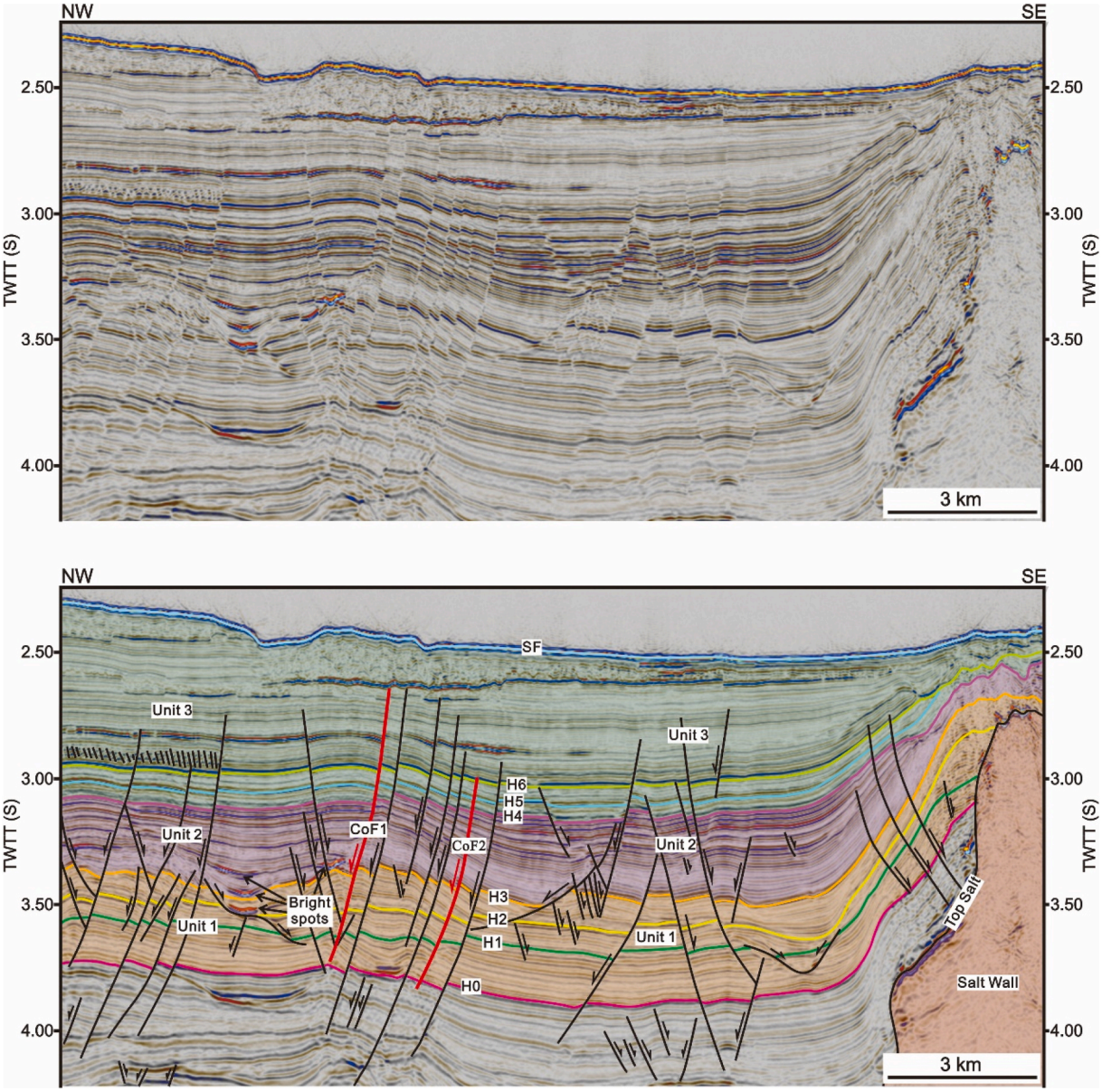

Fig. 6. Seismic profiles showing representative corridor faults 1 (CoF1) and 2 (CoF2) in the study area. Red bold and black lines represent faults, while the other coloured lines mark the seismic-stratigraphic horizons interpreted in the study area. Bright spots are indicated in the figure. The location of the seismic profile is shown in Fig. 3. SF=Seafloor. (For interpretation of the references to colour in this figure legend, the reader is referred to the Web version of this article.)

3500 m. In addition, the rose diagrams and histograms of strike and dip of each fault family were plotted by using fault-point data on Move, and the radius value of the rose diagram is plotted as a ratio (Fig. 10). The fault-point data were received by discretising faults that were interpreted on Schlumberger's Petrel® into facets, and time-depth conversions were implemented for these data on Move®.

Later in our workflow, eight representative faults from the four interpreted fault families were selected to compile displacement-length along fault (D_{max}-L) and displacement-depth (D-Z) plots, which were used to evaluate fault growth history in the investigated minibasin (Figs. 11–14). Fault displacement was calculated using trigonometry rules to discern the throw and heave for a fault, considering the fault as a pure dip-slip fault. Listric faults record a large amount of horizontal offset (heave) and using throw would be a limiting over-simplification in our analysis.

The relationship between maximum displacement (D_{max}) and length (L) of a fault trace provides insights into the mechanisms of fault initiation, growth and evolution through time (Watterson, 1986; Walsh and Watterson, 1988; Peacock and Sanderson, 1991; Cowie and Scholz, 1992; Kim and Sanderson, 2005). The relationship between fault displacement (D) and depth (Z) provides insights into fault reactivation or nucleation positions (Mansfield and Cartwright, 1996; Cartwright and Mansfield, 1998; Baudon and Cartwright, 2008a; Baudon and cartwright, 2008b).

Stress inversions were completed using the Stress Analysis Module on Move®, which is based on the direct inversion method of Angelier (1990) by using dip-slip data of the interpreted faults including dip and dip azimuth. We estimated the orientation and distribution of palaeostress tensors responsible for the formation of each fault family observed in the study area, with the exception of listric faults. Listric and keystone faults were formed under the same stress field in the minibasin, suggesting that the palaeostress tensors obtained from keystone faults can be applied to listric faults.

Slip tendency and leakage factors were also computed in Move's® Stress Analysis Module using the palaeostress azimuths obtained from stress inversions. For this stage in our analysis, faults and horizons

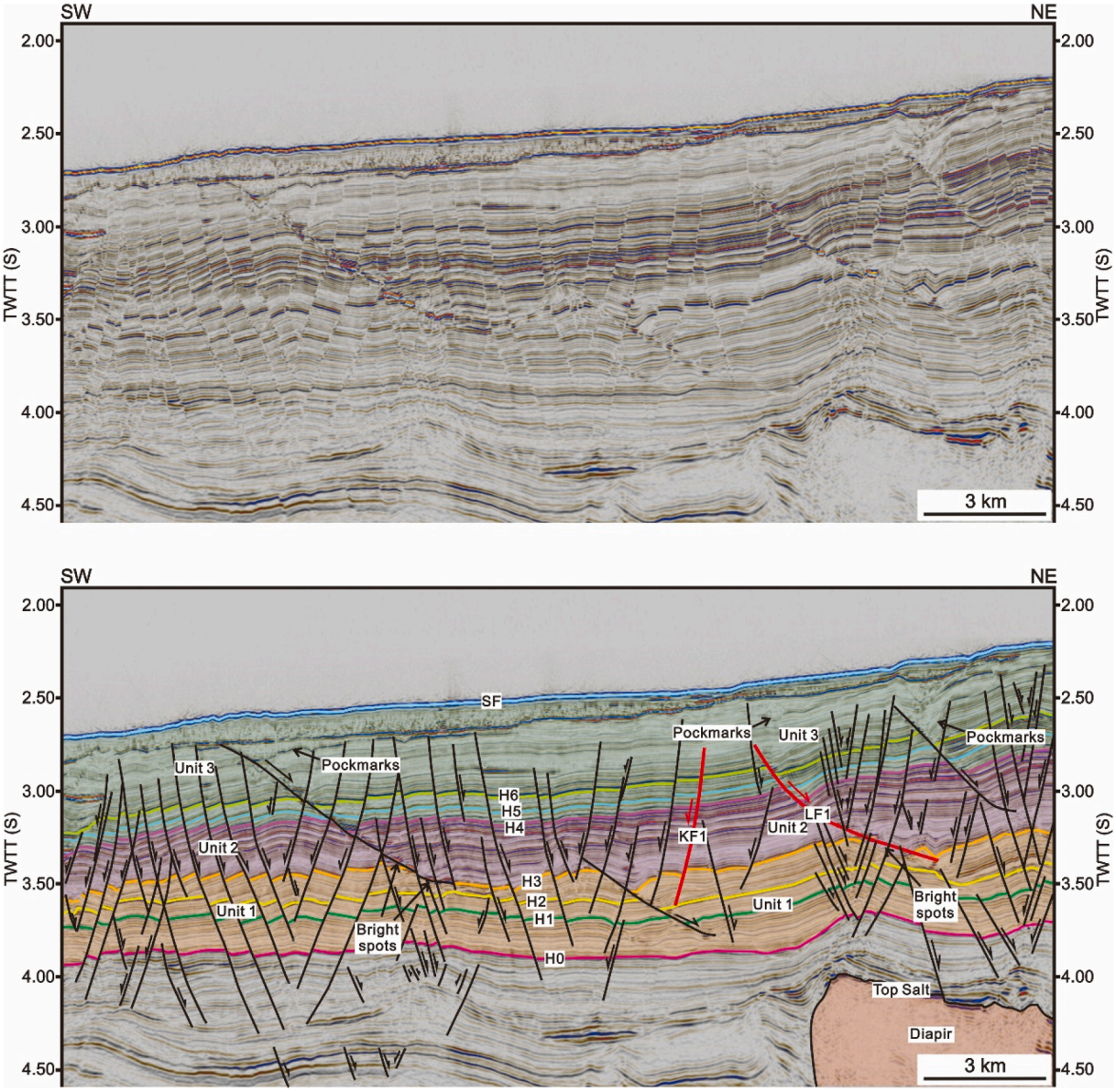

Fig. 7. Seismic profiles showing representative listric fault 1 (LF1) and keystone fault 1 (KF1). Red bold and black lines represent faults, while other coloured lines mark the different seismic-stratigraphic horizons interpreted in the study area. Bright spots and pockmarks are indicated in the figure. The location of the seismic profile is shown in Fig. 3. SF=Seafloor. (For interpretation of the references to colour in this figure legend, the reader is referred to the Web version of this article.)

interpreted in Petrel® were imported into Petroleum Experts Move® as 3D mesh surfaces, and later filtered for edge triangles. Key fault attributes, including true dip, strike and azimuth for each fault vertex, were created in Move® using the Attribute Analyser Toolbar. In addition, normalised leakage factors values were also calculated for each fault family, estimating favourable fluid pathways amongst the four fault families. As the palaeostress tensors obtained from stress inversion are not those representing the present-day stress regime, slip tendency and leakage factor analyses in this work comprise certain limitations, and do not fully indicate the most favourable fluid pathways in the study area at present. However, they represent the stresses that generated the faults interpreted in this work, and highlight any changes in the azimuth of such stresses in time and space, in the study area.

Slip tendency (T_s) indicates the likelihood of a fault to slip, and is defined as the ratio of resolved shear (τ) to normal stress (σ_n) (Equation (1); Morris et al., 1996; Lisle and Srivastava, 2004). It has no units and ranges from 0 to 1, where higher values indicate a higher likelihood of a fault to slip. It is dependent on the differential stress ratio and on the orientation of the fault surface in relation to the orientation of a given stress field. Therefore, the slip tendency can be expressed as:

$$T_s = \tau/\sigma_n \quad (1)$$

Leakage factor (L) is a measure of the fluid transmissivity of faults, and is defined as the ratio of pore pressure (P_p) to the difference between normal (σ_n) and shear stresses (τ) on a particular fault surface (Equation (2); Mattos and Alves, 2018; Ze and Alves, 2021). Pore pressure used in this study is the normal hydrostatic pressure calculated based on the depth we consider the fault have first nucleated. Leakage factor determines the likelihood of fault-seal failure; the higher the value, the greater the likelihood of a fault to act as a pathway for fluid. Therefore, the leakage factor can be written as:

$$L = P_P / (\sigma_n - \tau) \quad (2)$$

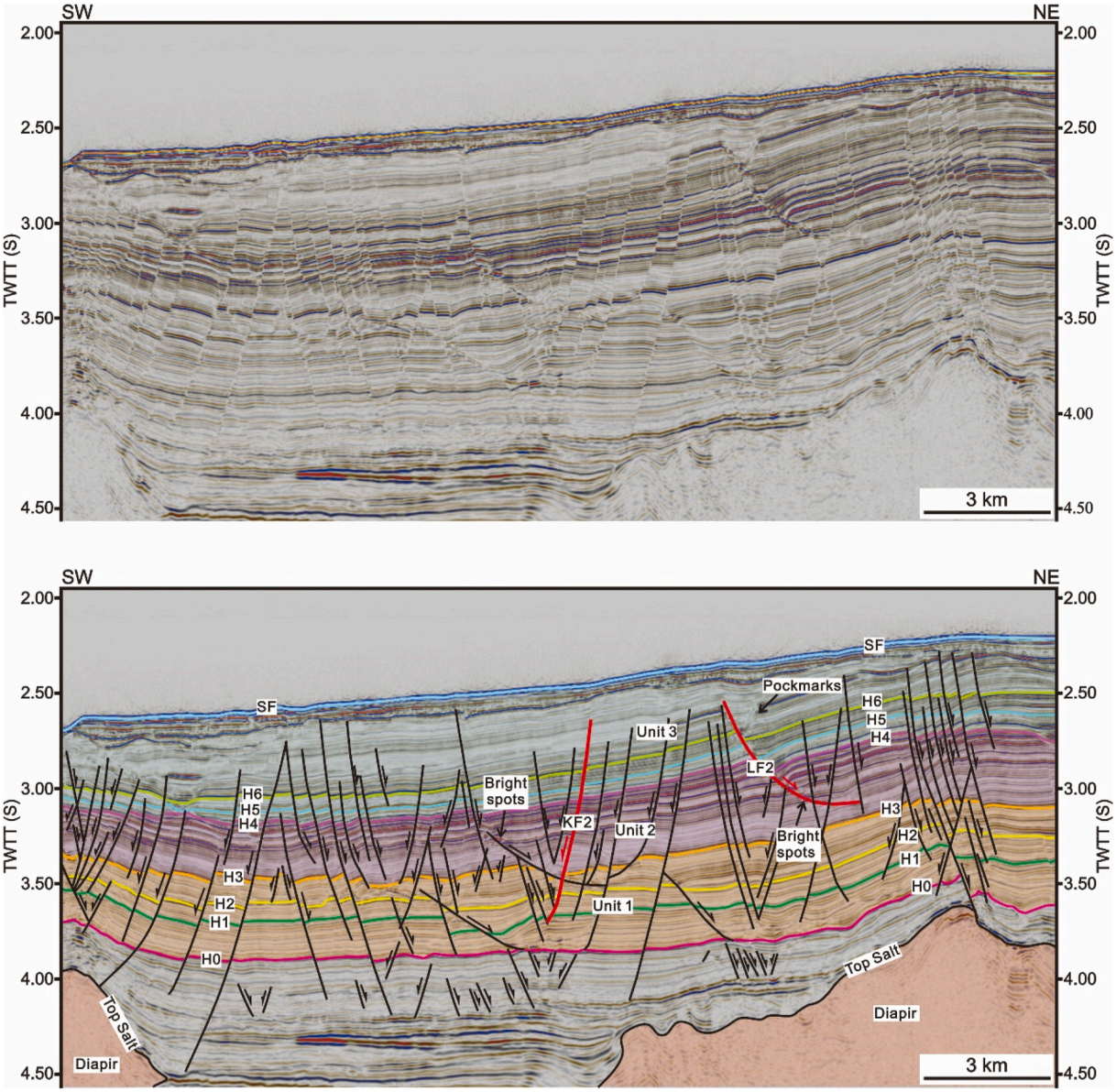

Fig. 8. Seismic profiles showing representative listric fault 2 (LF2) and keystone fault 2 (KF2). Red bold and black lines represent faults, while other coloured lines mark the different seismic-stratigraphic horizons interpreted in the study area. Bright spots and pockmarks are also indicated in the figure. The location of the seismic profile is shown in Fig. 3. SF=Seafloor. (For interpretation of the references to colour in this figure legend, the reader is referred to the Web version of this article.)

4. Seismic stratigraphy

4.1. Unit 1 (horizons H0 to H3)

Unit 1 is the primary seismic interval of interest, comprising a package of low amplitude to transparent seismic reflections somewhat similar to its underlying suprasalt strata (Figs. 5–8). The base of Unit 1 is marked by horizon H0, a low-to moderate-amplitude negative reflection tied to the base of Paleocene strata, whereas its top is bounded by a high-amplitude negative reflection defined as horizon H3 (Figs. 5–8). Between horizons H0 and H3, we mapped two other horizons (H1 and H2) with moderate-amplitude positive reflections (Figs. 5–8). These two horizons (H1 and H2) divide Unit 1 into three different sub-units, respectively named Unit 1a, 1b and 1c (Figs. 5–8). The amplitude of internal reflections in Unit 1a is slightly higher than in Unit 1b and 1c (Figs. 5–8). Faulting is common inside Unit 1, but most faults do not propagate below its lower boundary (horizon H0). This is likely due to the relatively higher ductility of strata in Unit 1 when compared to the intervals above and below, a character resulting in faults terminating at this level. Unit 1 is up to 600 ms thick in the salt minibasin of interest, but this value decreases slightly towards the flanks of adjacent salt structures (Fig. 9).

Unit 1 is composed of shale in its upper part (Unit 1b and 1c) and marl in its lower part (Unit 1a), with varying thickness and relative proportions of shale vs. marl at various locations (Fig. 4). Thin mudstone layers occur as intercalations in the essentially marly Unit 1a. Due to lithological changes, gamma-ray values reveal significant variations at depth. Unit 1b and 1c record high gamma-ray values, especially Unit 1c, but they gradually decrease towards the base of Unit 1b. Importantly, there is an increase in gamma-ray values from Unit 1a to 1b, and this increase correlates with the boundary between shale to marl in well data (e.g., well 1-BRSA-1143D; Fig. 4). Unit 1a presents higher gamma-ray values than Units 1b and 1c above, indicating Unit 1a contains a higher volume of shale than these former. In addition, gamma-ray values continue to increase below horizon H0 towards the top of the Aptian salt, although values in Unit 1 are similar to the underlying suprasalt

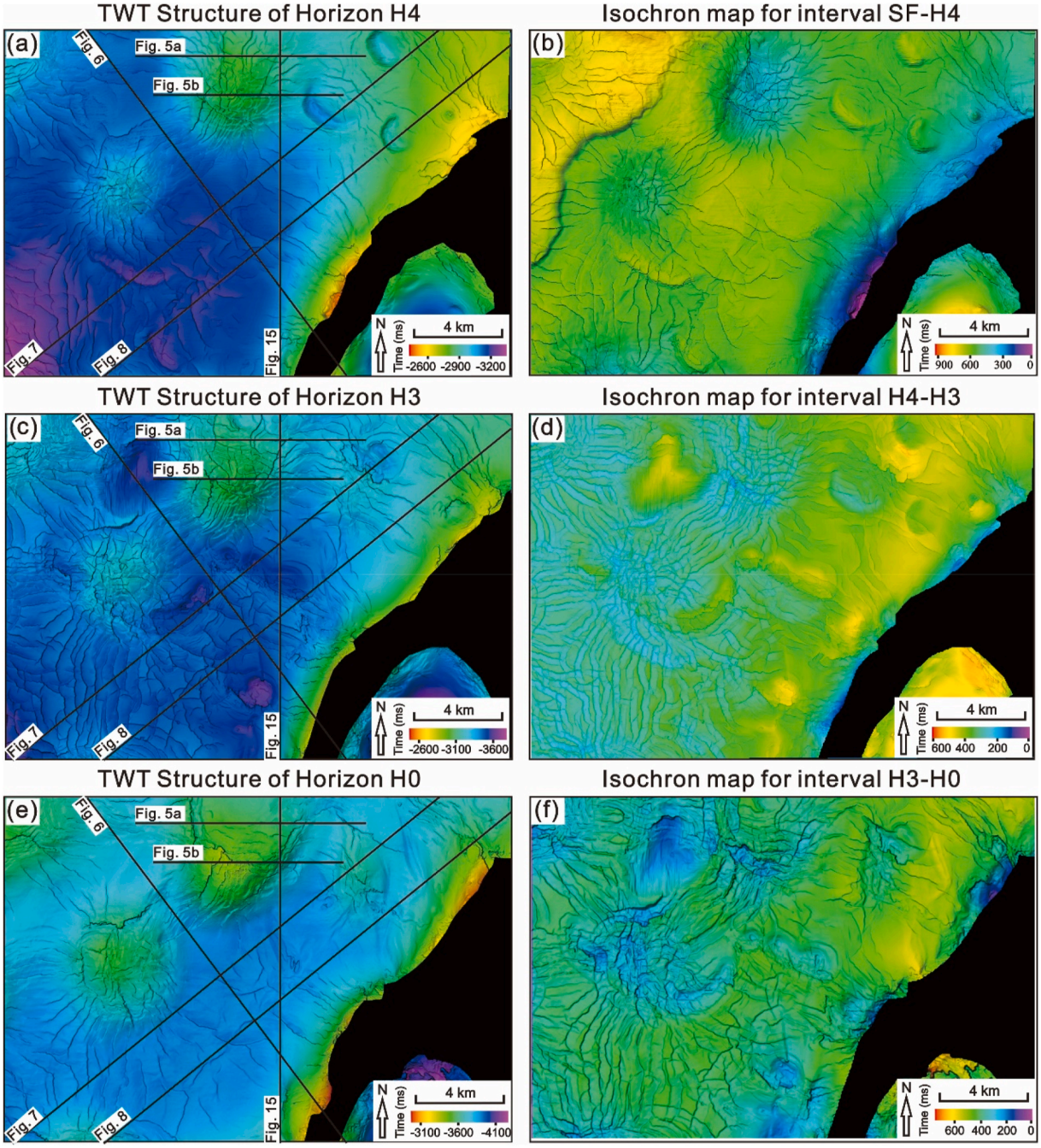

Fig. 9. TWT structural and isochron maps for representative horizons and intervals in the study area. a), c), and e) TWT structure of horizons H4, H3, and H0, respectively. b), d), and f) Isochron maps for intervals between the SF (seafloor) and horizon H4, between horizons H4 and H3, and between horizons H3 and H0.

strata (Fig. 4).

4.2. Unit 2 (horizons H3 to H4)

Unit 2 is bounded at its base by horizon H3, and at the top by horizon H4, a moderate-to high-amplitude positive reflection (Figs. 5–8). At the middle of Unit 2 there is one high-amplitude negative reflection that correlates with the base of Eocene strata (Figs. 5–8). This unit comprises a 200–500 ms thick package, which is the thickest (~500 ms) in the studied salt minibasin (Fig. 9). Unit 2 is the thinnest (~200 ms) above the salt diapirs (Fig. 9). The unit shows low-amplitude to transparent seismic reflections in its lower part, but its upper part is marked by moderate-to high-amplitude seismic reflections. Faulting is common, with most faults propagating upwards and downwards into Unit 2.

The lithology of Unit 2 is very similar to the interval between horizon H1 and H3 (Unit 1b and 1c), as both are composed of shale. However, Unit 2 does not show marked changes in lithology and gamma-ray curves remain high and relatively constant (Fig. 4).

4.3. Unit 3 (horizon H4 to the seafloor)

Unit 3 is bounded at its base by horizon H4, whereas its top coincides with the seafloor. Its thickness ranges from 400 to 800 ms, and shows low-amplitude to transparent internal reflections incised by submarine channels in some areas (Figs. 5–8). Two other horizons H5 and H6 were interpreted in this unit. Horizon H5 is a high-amplitude positive seismic reflection tied to the base of the Miocene, which is located two reflections above horizon H4 (Figs. 5–8). Horizon H6 is a high-amplitude

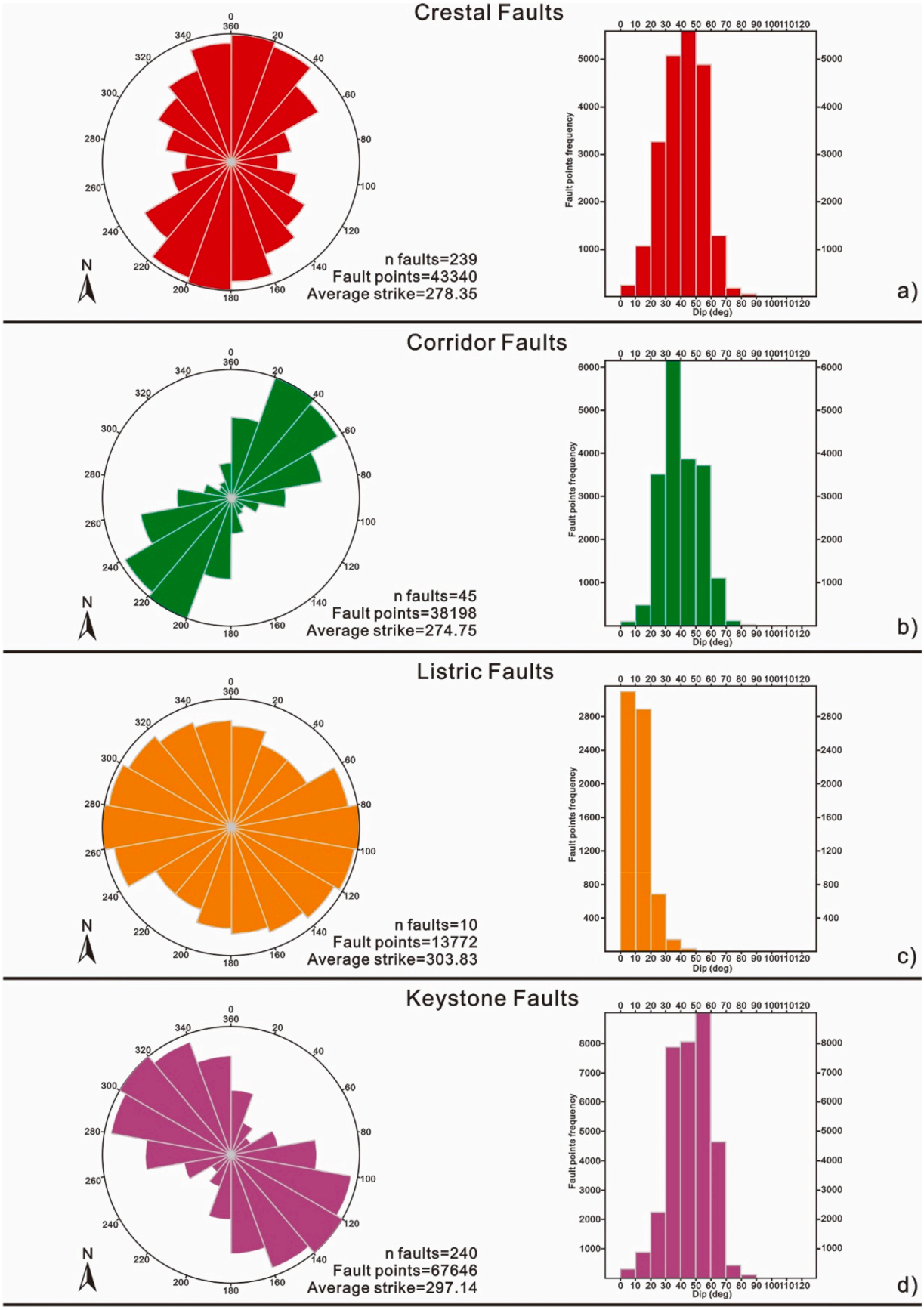

Fig. 10. Rose diagrams and histograms of strike and dip for each fault family in the study area plotted by using fault-point data. Crestal faults are predominantly NNE-striking and their dips range from 22.63° to 58.67°. Corridor faults are NE-striking and their dips vary from 23.77° to 58.21°. Listric faults are mainly NW-striking, but their dips range from 2.3° to 22.88°. Keystone faults are NW-striking with dips varying from 29.71° to 63.97°.

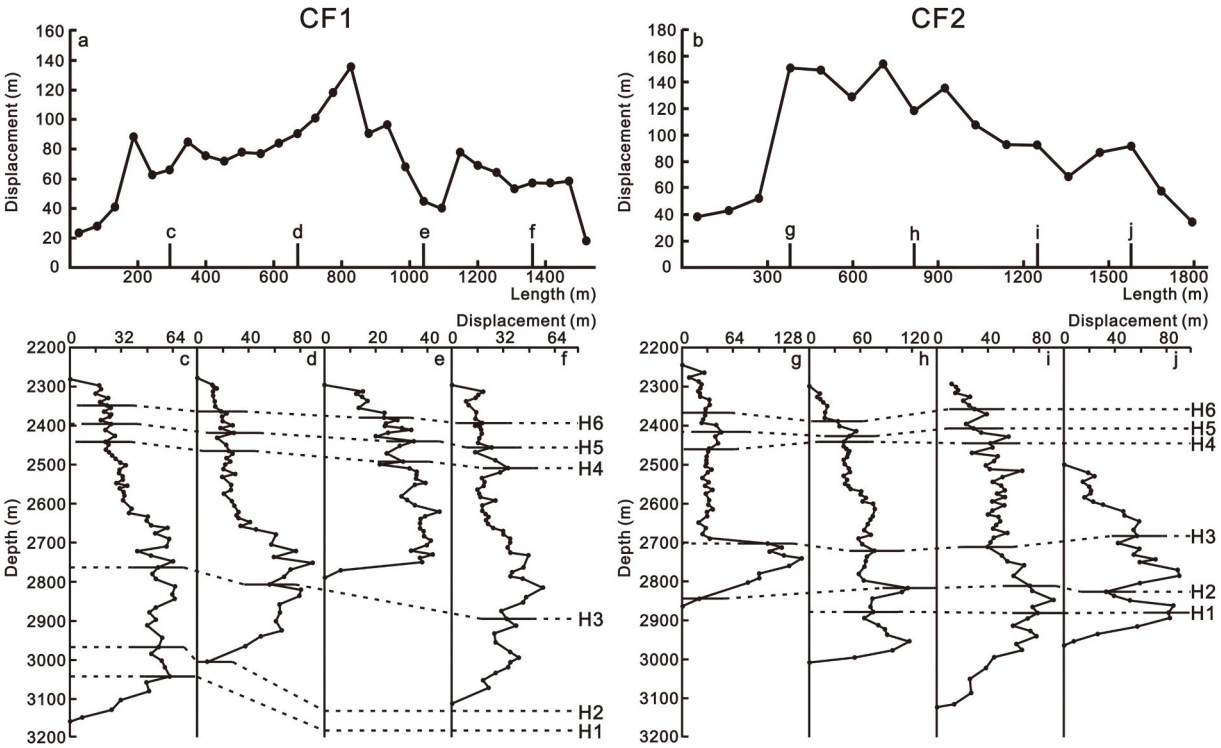

Fig. 11. Displacement-length along fault (D_{max}-L) and displacement-depth (D–Z) plots of crestal faults 1 (CF1) and 2 (CF2) highlighted in Figs. 3 and 5. The vertical lines c-j in the D-L plots above indicate the location of the D-Z plots shown below. The dashed lines mark the seismic-stratigraphic horizons interpreted in this study.

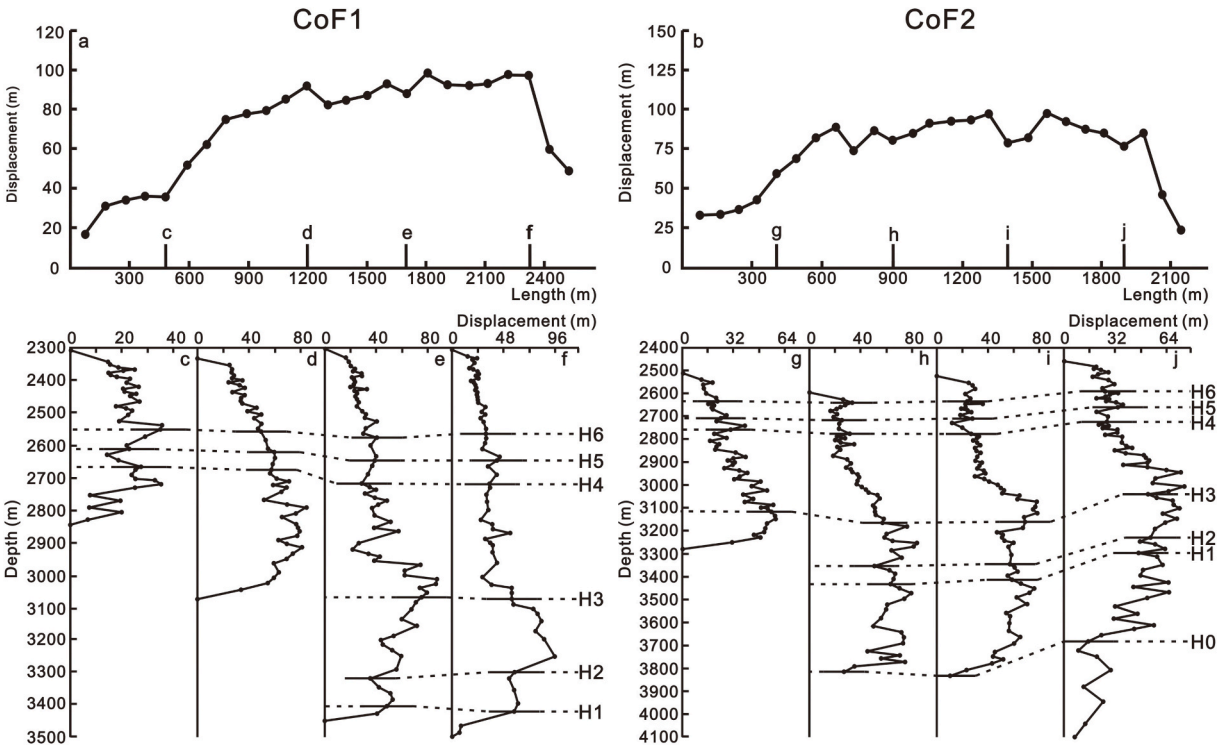

Fig. 12. Displacement-length along fault (D_{max}-L) and displacement-depth (D–Z) plots of corridor faults 1 (CoF1) and 2 (CoF2) imaged in Figs. 3 and 6. The vertical lines c-j in the D-L plots above indicate the location of the D-Z plots shown below. The dashed lines mark the seismic-stratigraphic horizons interpreted in this study.

positive reflection under another prominent high-amplitude negative reflection (Figs. 5–8). Most faults in the study area offset horizons H4 to H6, and many are truncated on their upper tips by mass-transport deposits (MTDs), which mark the remobilization of seafloor strata due to the influence of gravity forces.

Unit 3 is mainly composed of clay and shows high, relative constant gamma-ray values in its lower part, especially between horizons H4 and H6 (Fig. 4). Its top part comprises a large volume of turbidites, which

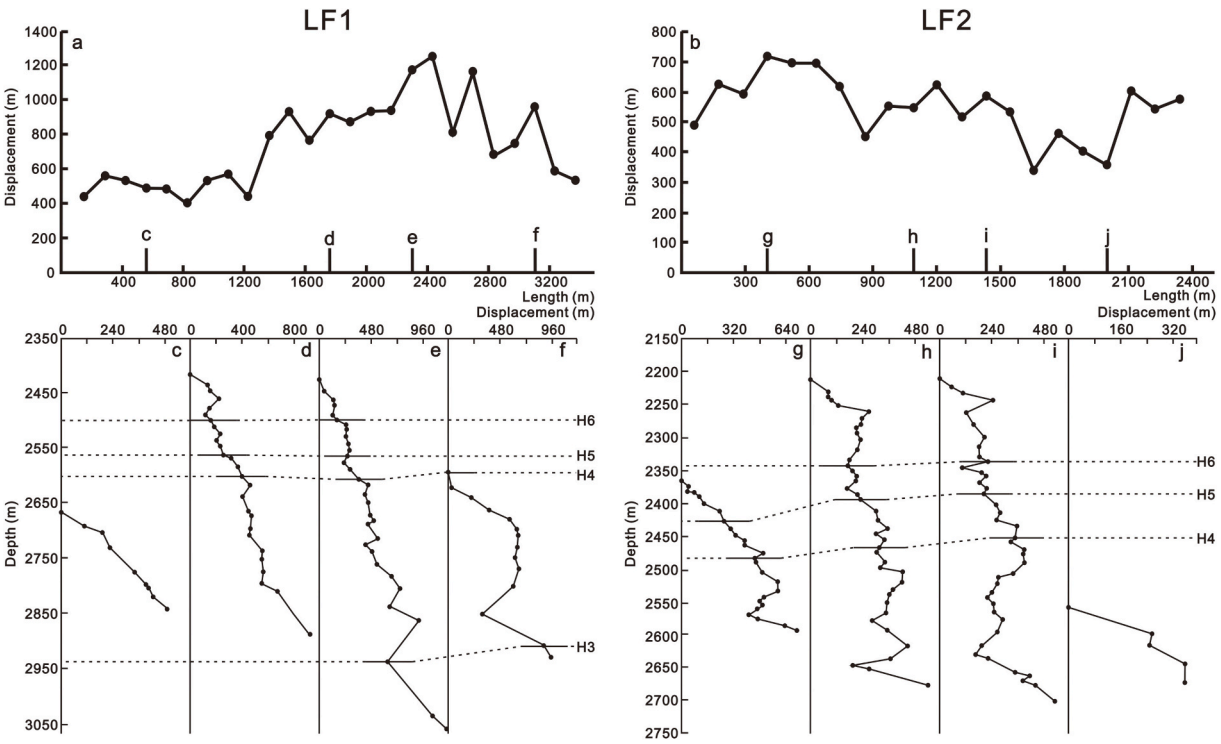

Fig. 13. Displacement-length along fault (D_{max}-L) and displacement-depth (D–Z) plots of listric faults 1 (LF1) and 2 (LF2) imaged in Figs. 3, 7 and 8. The vertical lines c-j in the D-L plots above indicate the location of the D-Z plots shown below. The dashed lines mark the seismic-stratigraphic horizons interpreted in this study.

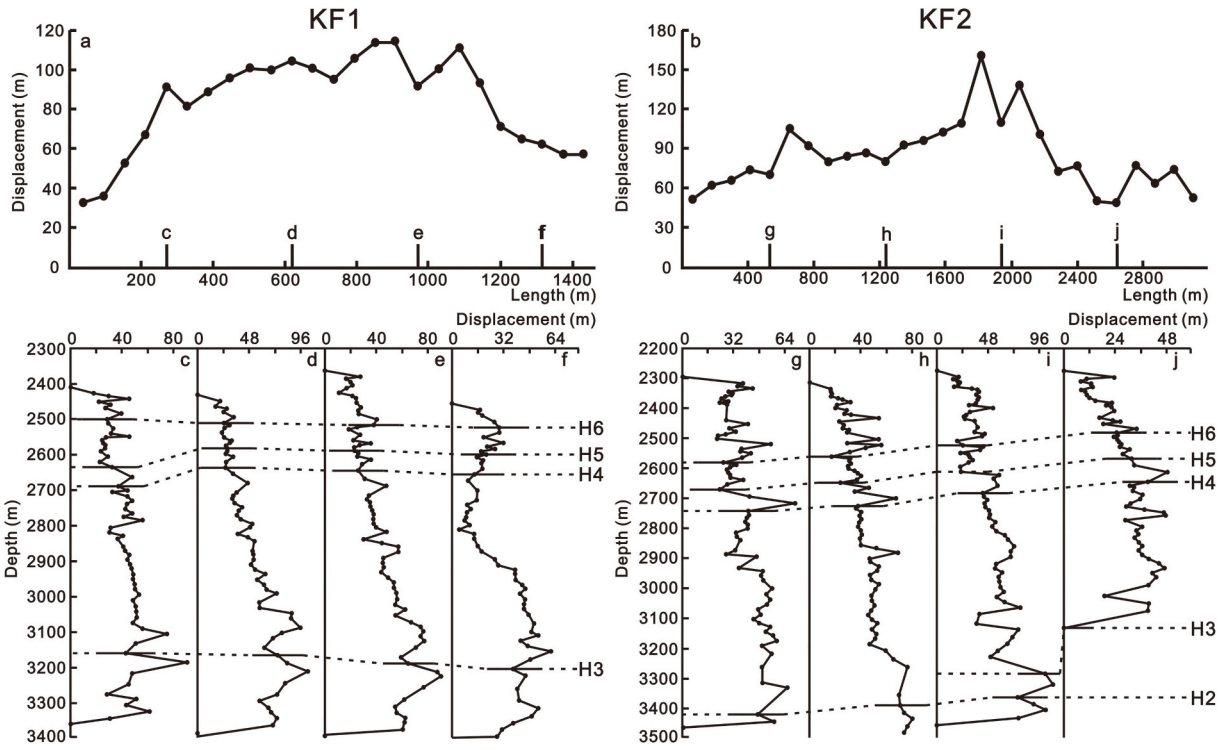

Fig. 14. Displacement-length along fault (D_{max}-L) and displacement-depth (D–Z) plots of keystone faults 1 (KF1) and 2 (KF2) imaged in Figs. 3, 7 and 8. The vertical lines c-j in the D-L plots above indicate the location of the D-Z plots shown below. The dashed lines mark the seismic-stratigraphic horizons interpreted in this study.

present relative low gamma-ray values.

5. Fault families around salt structures

Faults developed in the study area comprise four (4) fault families based on their geometry, orientation, distribution and relationship with

main salt structures: a) crestal faults, b) corridor faults, c) listric faults, and d) keystone faults (Figs. 3 and 10). Crestal faults include radial and concentric faults developed above salt structures due to halokinesis. Corridor faults pertain to faults connecting different salt structures, forming structural corridors that are preferential pathways for fluid (Mattos and Alves, 2018). Keystone and listric faults were developed in salt minibasins, but their geometries and periods of activity showed significant differences. In this section, we select eight (8) representative faults from the four fault families to compile displacement-length (D_{max}-L) and displacement-depth (D-Z) plots (Figs. 11–14). These data are used to evaluate the growth history of faults.

5.1. Crestal faults

A total of 239 crestal faults were manually mapped over salt diapir A, which is located in the northern part of the study area (Fig. 3). Crestal faults are well developed above this diapir, offsetting horizons H4 to H6 upwards to a depth just below a near-seafloor MTD (Figs. 3 and 5). Downwards, they terminate in Unit 1 to form graben structures above diapir A (Fig. 5). Crestal faults strike towards the NNE and have dips over 42° (Figs. 9 and 10).

Crestal faults 1 (CF1) and 2 (CF2) are respectively 1.5 km and 1.8 km long, N-striking, but show opposite dips; CF1 dips to the east, while CF2 dips to the west (Fig. 5). Their maximum displacement reaches 135 m and 153 m, respectively (Fig. 11). Crestal fault CF1 grew by the lateral linkage of distinct segments, as shown by the rugged profile of its D_{max}-L plot. A prominent linkage point is located around the position of profile e (Fig. 11). It is also clear from our D-Z data that the maximum displacement of CF1 occurs around horizon H3, with a decrease in displacement occurring between horizons H3 and H4 (Fig. 11). This suggests fault reactivation during the deposition of Unit 2.

Crestal fault CF2 is an isolated fault revealing a rugged 'C' type in D_{max}-L data (Fig. 11b). However, similarly to CF1, it shows multiple displacement minima values, implying that it was formed by dip linkage. The maximum displacement of CF2 occurs below horizon H3, showing that it first nucleated at this depth (Fig. 11). Interestingly, there are marked drops in displacement around horizon H3, especially around the position of profile g (Fig. 11g), suggesting that fault reactivation occurred at this level.

5.2. Corridor faults

Forty-five (45) corridor faults were recognised in the region between salt diapirs A and B, in the northwest part of the study area (Fig. 3). Corridor faults are NE-striking, with dips over 39°, and offset strata between horizons H1 to H6 (Figs. 6 and 10). Some large corridor faults also offset strata at horizon H0 and below (Fig. 6). They strike in a similar direction to the radial faults formed between diapirs A and B (Figs. 3 and 9).

Corridor faults 1 (CoF1) and 2 (CoF2) were chosen as representative corridor faults in the study area (Fig. 3). They are 2.5 km and 2.2 km long and dip to the northwest, with displacement maxima of 97 m and 99 m, respectively (Fig. 12). CoF1 offsets strata between H1 and terminates below the near-seafloor MTDs, while CoF2 offsets strata between H0 and H6. Both faults are single, isolated faults, as they have typical 'C-type' profiles in D_{max}-L plots (Fig. 12). Their displacement maxima occur around horizon H3, indicating they nucleate around horizon H3. In addition, both faults record a decrease in displacement between horizons H3 and H4 (Fig. 12). This suggests that fault reactivation occurred at the level of Unit 2.

5.3. Listric faults

Ten (10) listric faults were mapped as NW- to WNW-striking structures dipping to the northeast (Figs. 3 and 7–9). In plan-view, listric faults are curved, show variable lengths, and are cross-cut by adjacent faults (Figs. 3 and 9). On vertical seismic profiles, they are steep in their upper part but gradually sole out into Unit 1 (Figs. 7 and 8). Their dip ranges from 2° to 23° (Fig. 10), as they are gentler than the other fault families. Most listric faults are growth faults, i.e. they show thickening in strata adjacent to hanging-wall depocenters, a character that can be used to indicate their relative ages (Childs et al., 2003, 2017). Listric faults also reveal larger displacements when compared to the other fault families; they can be interpreted as structures accommodating extension along a NE-SW direction (Figs. 9 and 13).

Representative listric faults 1 (LF1) and 2 (LF2) are 2.4 km and 3.2 km long, with displacement maxima of 1254 m and 717 m, respectively (Figs. 9 and 13). They offset strata between horizons H4 and H6, soling out in the uppermost part of Unit 1 (Figs. 7, 8 and 13). Both listric faults are offset by other faults, especially LF1, indicating they were formed earlier than the faults that offset them. Because of these offsetting faults, LF1 and LF2 show rugged shapes in their D_{max}-L plots (Fig. 13). For instance, the marked displacement minima recorded between horizons H3 and H4 in D-Z profiles were also caused by younger faults offsetting them (Fig. 13). Displacement maxima in both LF1 and LF2 are recorded between horizons H3 and H4, implying the two faults nucleated at this depth (Fig. 13). Interestingly, the positions of displacement maxima are recorded close to the listric faults' lower tips (Figs. 7, 8 and 13), indicating they were not formed by the linkage between a steeply dipping fault and a gently dipping detachment. They nucleated around their lower tips, and propagated upwards (with minor downward propagation) to generate their present-day curvature.

5.4. Keystone faults

Two-hundred and forty (240) keystone faults were mapped in the salt minibasin of interest and they offset variable strata spanning horizons H0 to H6 (Figs. 7 and 8). Keystone faults are mainly NW-striking, relatively steep (>46.8°), with a few NE-striking faults occurring in the southern part of the minibasin (Figs. 3 and 8).

Keystone faults 1 (KF1) and 2 (KF2) were chosen as representative faults in this work. They are 1.4 km and 3.1 km long, with displacement maxima of 114 m and 110 m, respectively (Fig. 14). Both faults strike to the NW and dip to the southwest; they are also relatively steep and offset strata between horizons H1 to H6 (Figs. 7 and 8). KF1 records a displacement maximum around horizon H3 (Fig. 14), indicating that it first nucleated at this level. There is also significant displacement minima below horizon H4 (Fig. 14f), suggesting KF1 might have experienced some degree of reactivation at this level. KF2 is formed by lateral segment linkage as there is significant displacement minima along its striking direction, which correlate with the linkage points observed in variance time-slices (Fig. 3). The maximum displacement value for KF2 occurs near horizon H2 (Fig. 14), showing it nucleated at this level.

6. 3D visualisation of listric faults and investigated relationship with specific shale units

Listric faults are well developed in the investigated salt minibasin and their lengths vary from 1.8 km to 4.9 km. They are also observed at different depths in the study area (Figs. 7–9 and 15). It is clear that listric faults developed in the south of the minibasin are deeper when compared to similar faults to the north (Figs. 7–9 and 15). In addition, growth strata reveal that listric faults in the south were formed earlier than those in the north. Two listric faults in the south of the minibasin were developed in Unit 1, with strata thickening in their hanging-wall depocenters (Fig. 15). In contrast, in the north of the minibasin, LF1 and LF2 sole out at the top interval of Unit 1 (Figs. 7 and 8), and growth strata indicate they were formed after the deposition of Unit 1.

A key characteristic is that all listric faults analysed in this work sole out at the level of Unit 1, a package of low amplitude to transparent seismic reflections (Figs. 7, 8 and 15). Furthermore, borehole data show that Unit 1 is composed of shale and marl with high gamma-ray values

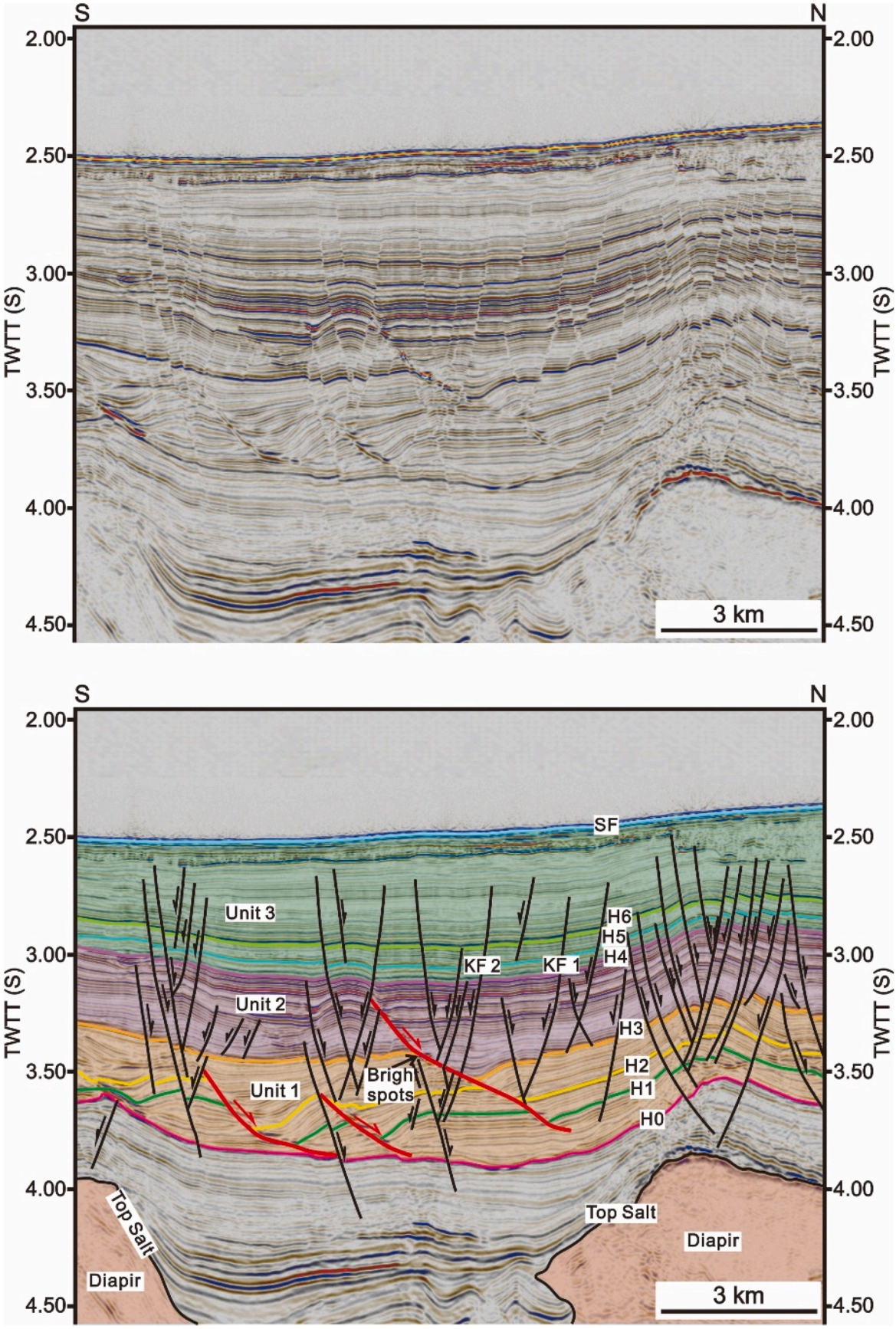

Fig. 15. Seismic profiles highlighting the distribution of listric faults in the study area. Red bold and black lines represent faults, while other coloured lines mark the different seismic-stratigraphic horizons interpreted in the study area. Bright spots are indicated in this figure. The location of the seismic profile is shown in Fig. 3. SF=Seafloor. (For interpretation of the references to colour in this figure legend, the reader is referred to the Web version of this article.)

(Fig. 4). Overpressure in Unit 1 is suggested by the existence of large pockmarks close to the upper tips of listric faults rooting at depth in this unit (Figs. 7 and 8). In fact, large-scale pockmarks have been previously considered to indicate the episodic loss of fluid due to overpressure build-up in underlying strata (Müller et al., 2018). Additionally, listric faults in the study area sole out into Unit 1, but they have not offset its lower boundary.

We interpret the formation of listric faults as related to local overpressure based on the mechanism proposed by Yuan et al. (2020). This may also explain the fact that listric faults in the south of minibasin formed earlier and deeper than those in the north, since Unit 1 is deepening to the south and local overpressures were putatively reached earlier in this part of the investigated salt minibasin when compared to its northern part.

7. Fluid-flow potential in distinct fault families

To understand the orientation and distribution of the principal palaeostress tensors in the study area, stress inversions were completed for all interpreted fault families. Stress inversion results for the 534 faults interpreted in the study area show a stress tensor with a sub-vertical σ_1 plunging 86.78° along an N39.21° azimuth. A sub-horizontal σ_2 plunges −2.07° along an N349.32° azimuth, accompanied by σ_3 plunging −2.46° along an N79.41° azimuth. However, as there are more than two preferential strike directions for faults in the study area due to halokinesis, we completed stress inversions separately for each fault family to obtain their own principal palaeostress tensors except listric faults (Table 1). Listric faults and keystone faults were formed under the same stress field in minibasin, and most listric faults were offset by keystone faults, suggesting that the palaeostress tensors obtained from keystone faults can be applied to listric faults. We thus used the stress inversions results described above to complement slip tendency and leakage factor analyses for each fault family (Figs. 16 and 17).

Slip tendency models reveal marked differences among the four interpreted fault families (Fig. 16). Keystone faults record the largest average slip tendency (0.65), with values varying from 0.38 to 0.95 (Fig. 16e). In addition, NW-striking keystone faults record significantly higher slip tendency values than NE-striking keystone faults, meaning that the former (keystone) faults have the highest probability to slip. Corridor faults show the second largest average slip tendency (0.63), with ranges in slip tendency similar to keystone faults, from 0.38 to 0.9 (Fig. 16c). Crestal faults have lower average slip tendency than corridor faults (0.55), and values range from 0.3 to 0.83 (Fig. 16b). Listric faults become the lowest average slip tendency (0.15), with values ranging from 0.06 to 0.25 (Fig. 16d). These observations suggest that listric faults have the lowest tendency to slip.

Normalised leakage factors were also calculated based on the stress tensor considered for each fault family, and they show similar trends to slip tendency (Fig. 17). The normalised leakage factor values for keystone faults mainly range from 0.45 to 0.95 with an average value of 0.72 (Fig. 17e), showing that these faults have the highest probability of conducting fluid among the four fault families. Corridor faults and crestal faults record similar average normalised leakage factor (0.71 and 0.66), with values ranging from 0.45 to 0.94 and 0.33 to 0.91, respectively (Fig. 17b and c). Listric faults show the lowest average normalised leakage factor (0.3), with values ranging from 0.11 to 0.56.

According to the data described above, we find that keystone faults record the highest values for slip tendency and normalised leakage factors, and NW-striking keystone faults show larger values than other directions of keystone faults. Corridor and crestal faults have similar values for slip tendency and leakage factor. Conversely, listric faults show the lowest values in both slip tendency and leakage factors. Importantly, the dip and depth of faults significantly influences the calculated slip tendency and leakage factor values, as high-angle and shallow faults record higher values for both parameters than low angle and deep faults.

8. Discussion

8.1. Significance of listric faults and their soling out intervals

One of the key questions arising from our study concerns the significance of listric faults in salt minibasins. As previously mentioned in this work, listric faults sole out in Unit 1, which is composed of shale and marl with high gamma-ray values, as documented in borehole data (Fig. 4). In addition, multiple bright spots, one known indicator of hydrocarbons, are observed in the lower part of listric faults (Figs. 7, 8 and 15), showing that the lower part of listric faults acts as a barrier or seal to hydrocarbons and other fluids. Large pockmarks are also observed close to the upper tip of listric faults, indicating the existence of local strata overpressures.

The strata in which listric faults sole out overlies the thick salt rocks, indicating that potential overpressure occurs in suprasalt strata. These overpressures may be caused by dehydration at smectite-illite transition depths, or by the generation of hydrocarbons from source rocks, both occurring after reaching specific threshold temperatures (Bruce, 1984). The suprasalt strata below Unit 1 were deposited in the early drift-stage, correlating with upper Cretaceous intervals in the Lower Urucutuca Formation (Fig. 2). They comprise Cenomanian to Turonian transgressive marine deposits with type III kerogen, capable of producing high-API oils and gas (Mello and Maxwell, 1990; Fiduk et al., 2004). This kerogen should have reached thermal maturity - though buried at a relative shallow depth of around 1300–2000m - because a major thermal pulse in the early to middle Eocene has been recognised on multiple well data from the continental shelf. This thermal pulse is associated with the emplacement of the Abrolhos volcanic Plateau (Meisling et al., 2001; Cobbold et al., 2001; Gibbs et al., 2003; Fiduk et al., 2004). Due to the presence of bright spots in the lower part of listric faults, we suggest that overpressure in the study area was caused by the cracking of hydrocarbons in Cenomanian to Turonian strata, which was locally heated due to the high thermal conductivity of underlying salt.

The lower Urucutuca formation is composed of shale and marl, and shows the highest gamma-ray values in the study area (Fig. 4). At the same time, it comprises low amplitude to transparent seismic reflections in seismic data (Figs. 5–8 and 15). The interval into which listric faults sole out have similar seismic, lithological and petrophysical characters to Lower Urucutuca strata (Figs. 5–8 and 15). In parallel, the interval in question was deposited in an evolving salt minibasin, in which strata is potentially rich in organic carbon due to its restricted ocean circulation

Table 1
Stress inversion values obtained considering the total number of faults and each fault family separately. Results from palaeostress inversions suggest a sub-vertical σ_1 and sub-horizontal σ_3.

Faults	Number of faults	σ_1		σ_2		σ_3	
		Plunge	Azimuth	Plunge	Azimuth	Plunge	Azimuth
Total faults (Including listric faults)	534	86.78	39.21	−2.07	349.32	−2.46	79.41
Crestal faults	239	88.84	55.97	−0.83	11.51	−0.81	101.53
Corridor faults	45	88.87	78.43	−0.92	42.95	−0.66	132.97
Keystone faults	240	−89.4	88.64	0.42	133.64	0.42	43.63

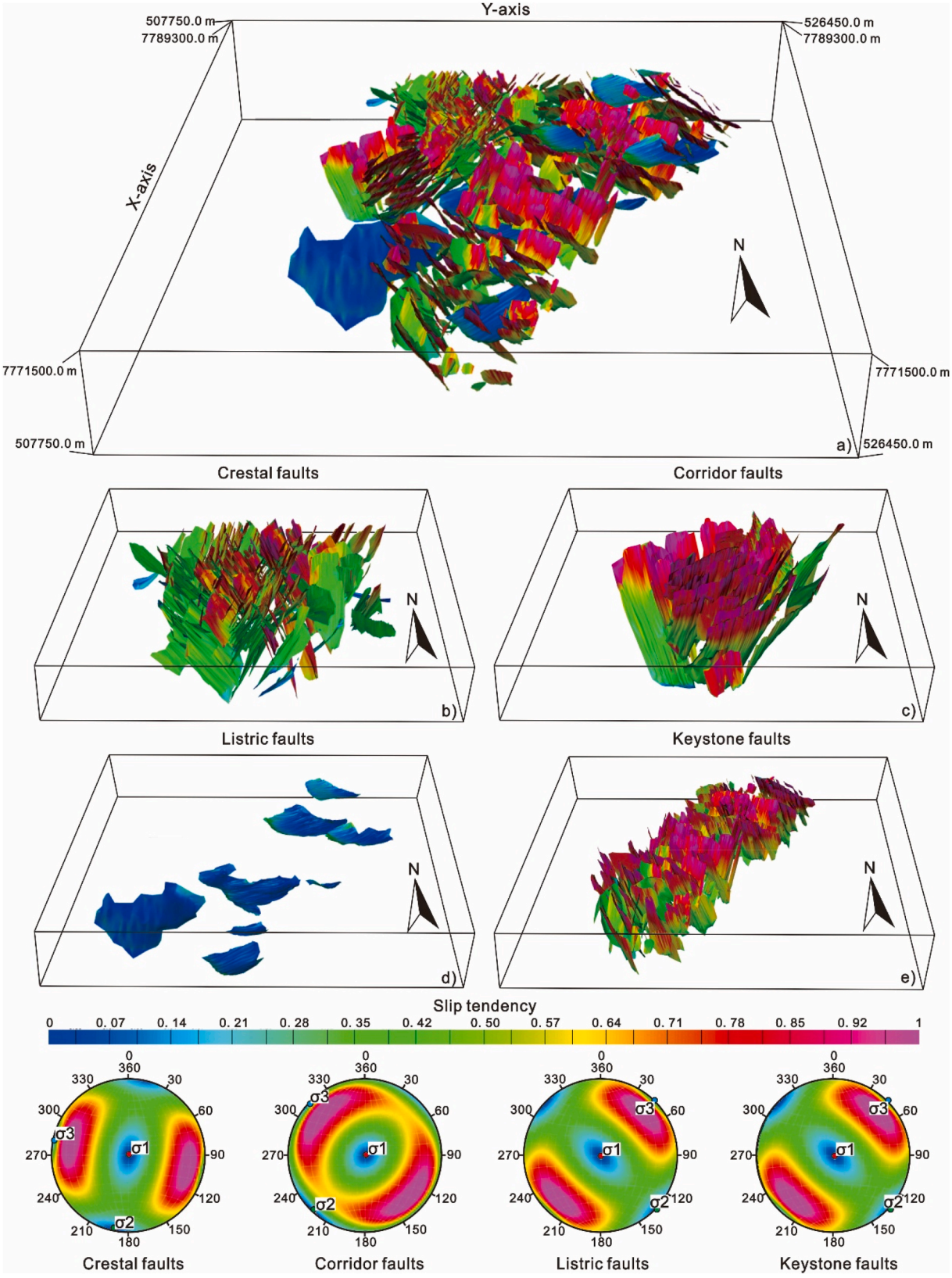

Fig. 16. a) Slip tendency analysis for the four fault families in this article considering the palaeostress tensor obtained separately from each family. b)-e) Slip tendency analysis for crestal, corridor, listric, and keystone faults.

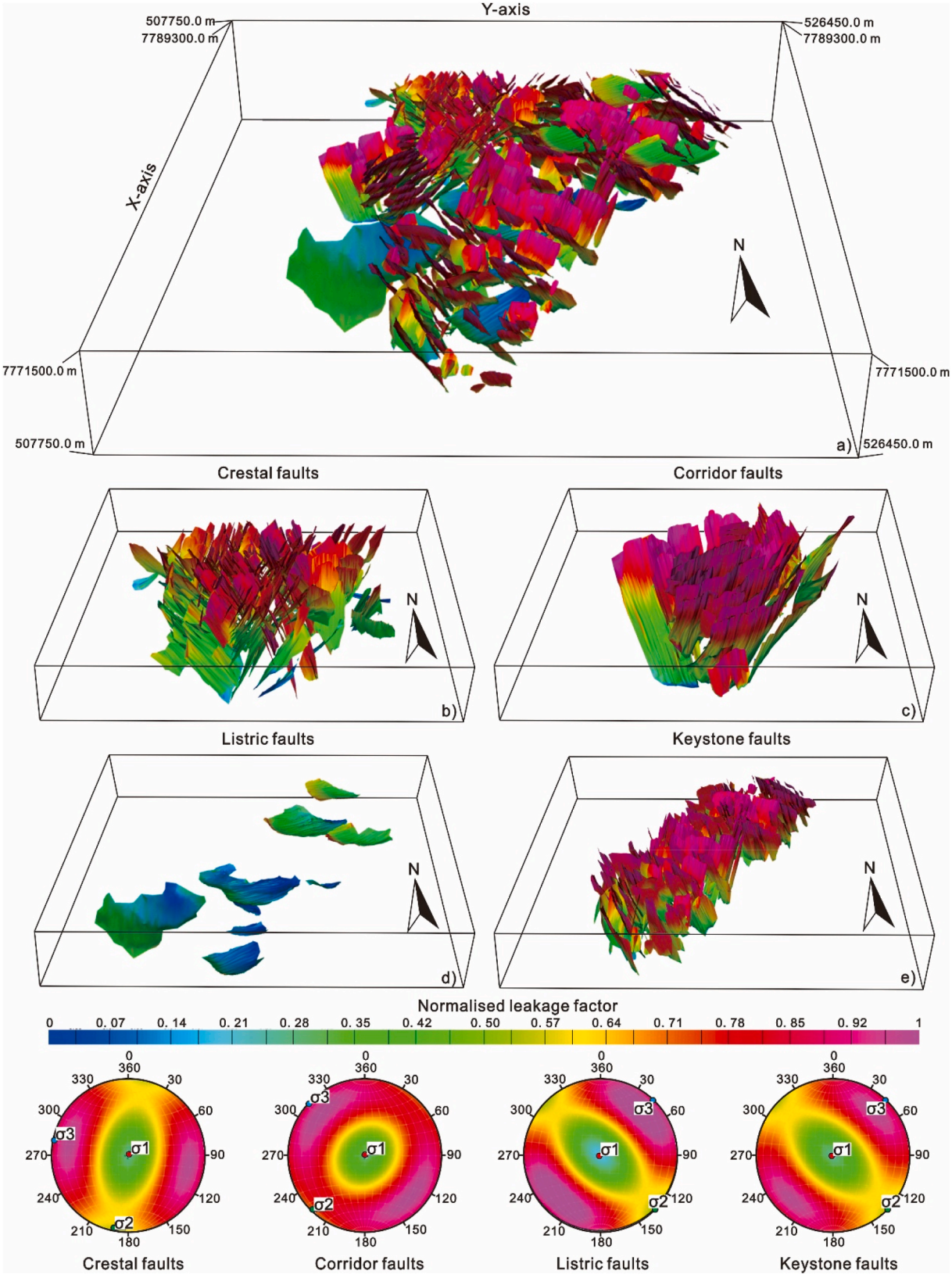

Fig. 17. a) Normalised leakage factor analysis for the four fault families in this article considering the palaeostress tensor obtained separately from each family. b)-e) Normalised leakage factor analysis for crestal, corridor, listric, and keystone faults.

(Dow, 1984; Lopez, 1990). Thus, it is highly likely that listric fault sole out in ductile, potentially organic-rich shales and marls, though drilled wells crossing such horizon did not provide total organic carbon (TOC) data. The soling out intervals directly overlie Lower Urucutuca source-rock intervals deposited in the Cenomanian-Turonian (Cobbold et al., 2001; Gibbs et al., 2003; Fiduk et al., 2004), suggesting these intervals may be added to the known source-rock potential of the Espírito Santo Basin.

8.2. *Faults as markers of distinct stages of halokinesis*

Tectonic faults are one of the most common brittle structures in sedimentary basins and provide important information about the evolution of a sedimentary basin. As part of a typical salt-bearing basin, the formation and evolution of faults in the study area have been strongly influenced by halokinesis. We have identified three evolutionary stages between horizon H0 and the seafloor in the study area, correlating to the drift stage of the Espírito Santo Basin (Fig. 18).

Stage 1 (Paleocene), between seismic horizons H0 and H3, is characterised by the formation of a few NW- or WNW-striking listric faults, keystone faults, and marks the onset of reactive diapirism in the study area. Several WNW-striking listric faults revealing significant strata thickening in their hanging walls were formed during this stage (Figs. 9 and 15), and accommodated displacement along a NE-SW direction. At this same time, NW- to WNW-striking keystone faults were also developed, implying the establishment of a NE-SW direction of extension. However, the activity of salt diapirs and walls was minor during Stage 1, as only few crestal faults and corridor faults were formed around these same structures. Corroborating this interpretation, the thickness of strata between horizons H0 and H3 is relatively constant in the study area (Fig. 10), and no significant erosion occurred on top of salt structures (Fig. 18a). The relatively weak halokinesis can be explained by the absence of significant sediment loading and, as a result, NE-SW extension predominated in the study area during Stage 1.

Stage 2 (Late Paleocene-Early Oligocene), marked by strata deposited between horizons H3 and H4, records active diapirism as a consequence of enhanced sediment loading over the salt, and lead to the development of crestal and NE-striking corridor faults (Fig. 18b). A few NE- and NW-striking keystone faults, plus NW-striking listric faults, were also developed during this stage. Halokinesis was intensified with increasing sediment loads, with salt diapirs and walls developing by active diapirism. NE-striking corridor faults started to form at this stage, synchronously with crestal faults. In contrast to Stage 1, strata are thicker in salt minibasins (up to 450 m) compared to the units accumulated on top of salt structures (less than 200 m), proving that significant erosion, or non-deposition, occurred above the latter. Importantly, the development of several NW-striking listric faults and multiple NW-striking keystone faults still denote a predominant NE-SW direction of extension in the investigated salt minibasin.

With continuing halokinesis, the salt underlying the minibasins was withdrawn to feed the surrounding salt diapirs and walls, promoting moderate extension along a NW-SE direction (Fig. 18b). This eventually formed NE-striking faults, which intersected the NW-striking keystone and listric faults. Such a cross-cutting relationship is obvious in the southern part of the main salt minibasin as large volumes of salt were withdrawn in this region. Conversely, in the northern half of the minibasin there is only one small salt diapir below horizon H3, leading to the generation of crestal faults with different strikes (Fig. 18b).

Stage 3 (Late Oligocene-Recent), spanning strata between horizon H4 and the seafloor, is characterised by more intense (active) diapirism due to increased sediment loading, a process resulting in the formation of multiple crestal faults around salt structures, NE-striking corridor faults, NW-striking keystone faults and NE-striking keystone faults. These faults present variable geometries, although the main salt minibasin was still controlled by a NE-SW direction of extension, as NW-striking keystone faults were developed during this stage. There was

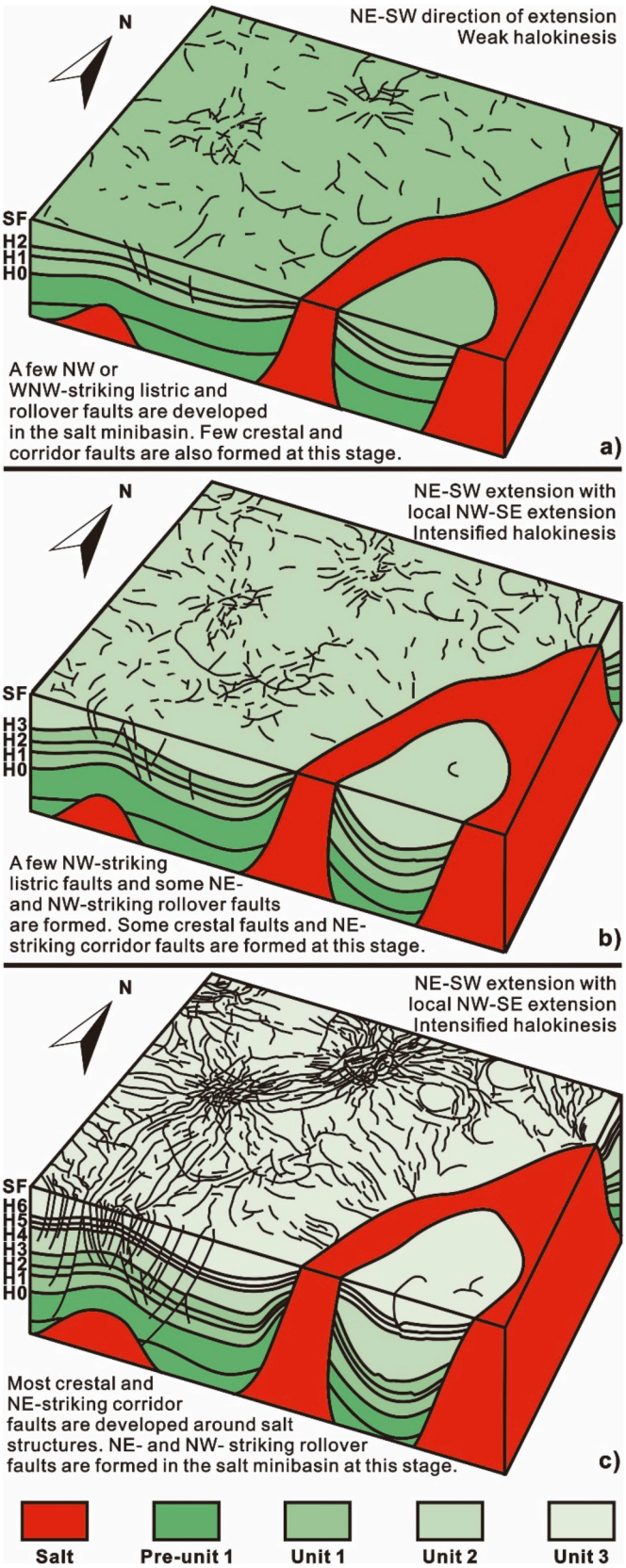

Fig. 18. Schematic block diagram model of the three evolution stages interpreted in the study area. a) Stage 1 (Paleocene); b) Stage 2 (Late Paleocene-Early Oligocene); c) Stage 3 (Late Oligocene-Recent).

also NW-SE extension in the southern part of the salt minibasin, which led to the generation of the NE-striking faults that intersect NW-striking keystone faults (Fig. 18c). In addition, these same keystone faults were formed after the listric faults considered in this work, and they offset the latter in the study area. Later in the evolution of the salt minibasin, a large mass-transport deposit (MTD) was accumulated near the seafloor due to widespread gravity spreading and downslope sediment movement (Figss. 4–7). In fact, MTDs exhibit a high variability in size and internal character in the study area (Biancardi et al., 2020), and truncate the upper tip of several faults, especially crestal faults developed above salt diapirs (Fig. 5).

8.3. *Implications for the establishment of favourable fluid pathways*

Faults can act as effective conduits for fluid in sedimentary basins but, conversely, they can also locally act as barriers to fluid along fault zones (Cox et al., 2001; Gartrell et al., 2004). In practice, it is commonly difficult to determine whether a fault acts as conduit or barrier to fluid flow, as its sealing competence is influenced by multiple factors such as the lithology of the strata crossed by the fault, its displacement, fault-gouge geometry, fault geometry in relation to local stress fields, post-deformation cementation, interactions between fluids and host rock, etc. (Caine et al., 1996; Fisher and Knipe, 2001; Koledoye et al., 2003; Manzocchi et al., 2010). In the study area, four (4) fault families are developed around salt structures, and it is of great importance to identify and model the favourable pathways for fluid migrating from deeper strata (e.g. Gartrell et al., 2004; Hovland, 2007; Davison, 2009; Andresen et al., 2011). Fault and fluid flow mapping can also be helpful to predict geohazards associated with fluid flow and seafloor leakage such as submarine slope instability, or the sudden formation of pockmarks and near-seafloor fluid pipes (Elger et al., 2018; Cartwright et al., 2021). In this study, a normalised leakage factor was estimated for each of the four fault families to provide information about which is the most favourable fluid pathways.

Normalised leakage factors are the highest for keystone faults, ranging from 0.45 to 0.95 for an average value of 0.73 (Fig. 15e). Keystone faults are thus highly likely to act as conduits for fluid. In addition, keystone faults were active during all three evolution stages considered in this work, propagating into Unit 1 – regarded as a potential source interval. This means keystone faults are more likely to contribute to the migration of fluid from deeply-buried source rocks to shallow reservoirs. Corridor and crestal faults show leakage factor values varying from 0.45 to 0.94 and 0.37 to 0.91, respectively, with average values of 0.71 and 0.66 (Fig. 17). The leakage factor values for corridor and crestal faults are similar to those of keystone faults, suggesting they are also likely to act as pathways for fluid. Most of these faults were formed during Stages 2 and 3 under the effect of active diapirism and have propagated at different depths, including into Unit 1. They were also developed on top of salt diapirs where hydrocarbon tends to accumulate, so the reservoirs close to the upper part of crestal faults and corridor faults are possible exploration targets.

Listric faults have the lowest normalised leakage factor value ranging from 0.11 to 0.56, with an average of 0.4, indicating that they are more likely to act as barriers and baffles to fluid. This character explains the multiple bright spots encountered in the lower part of listric faults. However, listric faults are usually growth faults in the study area, and were mainly formed during Stages 1 and 2. They continued to be active for a long period, promoting the leakage of fluid in their upper parts, and generating large pockmarks above their upper tips. Therefore, based on our leakage factor data, we propose that keystone faults constitute the most favourable fluid pathways in the study area. Corridor and crestal faults also show potential to form pathways for fluid flow, but listric faults are likely barriers to fluid, particularly in their lower parts.

9. Conclusions

This work aimed at understanding the distribution, evolution history and significance of different fault families in a salt minibasin, and any favourable fluid pathways offshore Espírito Santo Basin (SE Brazil). The main conclusions of this work can be summarised as follows:

a) Four fault families are identified based on their geometry, orientation, distribution and relationship with main salt structures. Crestal faults were formed around salt structures together with radial and concentric faults. Corridor faults were developed among discrete salt diapirs, linking them through long corridors of oriented, conjugate fault families. Listric and keystone faults were formed in salt minibasins and were related to important extensional stresses.
b) The development of listric faults can indicate the existence of subsurface overpressure in strata. Moreover, the intervals into which listric faults sole out comprise soft and ductile strata, which is high likely associated with source rocks. These intervals may be added to the known source-rock potential of a given basin, identifying their depth and relative thickness.
c) Three fault evolution stages are identified in the study area. Stage 1 records the formation of a few NW- and WNW-striking listric and keystone faults in response to the onset of reactive diapirism. Stages 2 and 3 mark a shift to active diapirism in the study area promoted by increasing sediment loading, and lead to the formation of crestal, corridor and keystone faults.
d) Normalised leakage factors show that keystone faults are the most favourable fluid pathways in the study area. Corridor and crestal faults also show potential as pathways for fluid. Conversely, listric faults are likely barriers and baffles to fluid, particularly in their lower parts.

Declaration of competing interest

The authors declare that they have no known competing financial interests or personal relationships that could have appeared to influence the work reported in this paper.

Acknowledgements

The authors would like to acknowledge the permission conceded by CGG for the use of seismic data and the Brazilian National Petroleum Agency (ANP) for the well data provided. We thank Cerys Biancardi and Gwen Pettigrew for helping our data interpretation and for managing software licenses. The first author would like to acknowledge CSC (China Scholarship Council) for providing a PhD scholarship during his studies at Cardiff University. Schlumberger (providers of Petrel®) and Petroleum Experts (Move®) are acknowledged for the provision of the academic licences to Cardiff University 3D Seismic Lab. Finally, we thank Associate Editor Bernard Colletta and two anonymous reviewers for their constructive reviews.

References

Alves, T., Fetter, M., Busby, C., Gontijo, R., Cunha, T.A., Mattos, N.H., 2020. A tectono-stratigraphic review of continental breakup on intraplate continental margins and its impact on resultant hydrocarbon systems. Mar. Petrol. Geol. 117, 104341 https://doi.org/10.1016/j.marpetgeo.2020.104341.

Alves, T.M., 2012. Scale-relationships and geometry of normal faults reactivated during gravitational gliding of Albian rafts (Espirito Santo Basin, SE Brazil). Earth Planet Sci. Lett. 331, 80–96. https://doi.org/10.1016/j.epsl.2012.03.014.

Alves, T.M., Cunha, T., 2018. A phase of transient subsidence, sediment bypass and deposition of regressive–transgressive cycles during the breakup of Iberia and Newfoundland. Earth Planet Sci. Lett. 484, 168–183. https://doi.org/10.1016/j.epsl.2017.11.054.

Andresen, K.J., Huuse, M., Schødt, N.H., Clausen, L.F., Seidler, L., 2011. Hydrocarbon plumbing systems of salt minibasins offshore Angola revealed by three-dimensional seismic analysis. AAPG Bull. 95, 1039–1065. https://doi.org/10.1306/12131010046.

Angelier, J., 1990. Inversion of field data in fault tectonics to obtain the regional stress—III. A new rapid direct inversion method by analytical means. Geophys. J. Int. 103, 363–376. https://doi.org/10.1111/j.1365-246X.1990.tb01777.x.
Bally, A., Bernoulli, D., Davies, G., Montadert, L., 1981. Listric normal faults: oceanologica acta. In: Proceedings of the 26th International Geological Congress. Geology of Continental Margins Colloque C3. Paris, July (1981), pp. 87–101.
Barker, P., Buffler, R., Gambôa, L., 1983. A seismic-reflection study of the Rio-Grande Rise. Initial Rep. Deep Sea Drill. Proj. 72, 499–517.
Baudon, C., Cartwright, J., 2008. Early stage evolution of growth faults: 3D seismic insights from the Levant Basin, Eastern Mediterranean. J. Struct. Geol. 30, 888–898. https://doi.org/10.1016/j.jsg.2008.02.019.
Baudon, C., cartwright, J., 2008b. The kinematics of reactivation of normal faults using high resolution throw mapping. J. Struct. Geol. 30, 1072–1084. https://doi.org/10.1016/j.jsg.2008.04.008.
Biancardi, C.A., Alves, T.M., Martins-Ferreira, M.A.C., 2020. Unpredictable geometry and depositional stacking patterns of mass-transport complexes in salt minibasins. Mar. Petrol. Geol. 120, 104522 https://doi.org/10.1016/j.marpetgeo.2020.104522.
Bose, S., Mitra, S., 2009. Deformation along oblique and lateral ramps in listric normal faults: insights from experimental models. AAPG Bull. 93, 431–451. https://doi.org/10.1306/12080808117.
Brown, A.R., 2011. Interpretation of Three-Dimensional Seismic Data. Society of Exploration Geophysicists and American Association of Petroleum Geology. https://doi.org/10.1306/M4271346.
Bruce, C.H., 1984. Smectite dehydration—its relation to structural development and hydrocarbon accumulation in northern Gulf of Mexico basin. AAPG Bull. 68, 673–683. https://doi.org/10.1306/AD461363-16F7-11D7-8645000102C1865D.
Bruhn, C.H., Walker, R.G., 1997. Internal architecture and sedimentary evolution of coarse-grained, turbidite channel-levee complexes, Early Eocene Regencia Canyon, Espirito Santo Basin, Brazil. Sedimentology 44, 17–46. https://doi.org/10.1111/j.1365-3091.1997.tb00422.x.
Brun, J.-P., Mauduit, T.P.-O., 2008. Rollovers in salt tectonics: the inadequacy of the listric fault model. Tectonophysics 457, 1–11. https://doi.org/10.1016/j.tecto.2007.11.038.
Caine, J.S., Evans, J.P., Forster, C.B., 1996. Fault zone architecture and permeability structure. Geology 24, 1025–1028. https://doi.org/10.1130/0091-7613(1996)024%3C1025:FZAAPS%3E2.3.CO;2.
Cainelli, C., Mohriak, W.U., 1999. Some remarks on the evolution of sedimentary basins along the Eastern Brazilian continental margin. Episodes 22, 206–216. https://doi.org/10.18814/epiiugs/1999/v22i3/008.
Cartwright, J., Kirkham, C., Foschi, M., Hodgson, N., Rodriguez, K., James, D., 2021. Quantitative reconstruction of pore-pressure history in sedimentary basins using fluid escape pipes. Geology. https://doi.org/10.1130/GEOL.S.13420394.
Cartwright, J., Lonergan, L., 1996. Volumetric contraction during the compaction of mudrocks: a mechanism for the development of regional-scale polygonal fault systems. Basin Res. 8, 183–193. https://doi.org/10.1046/j.1365-2117.1996.01536.x.
Cartwright, J., Mansfield, C., 1998. Lateral displacement variation and lateral tip geometry of normal faults in the Canyonlands National Park, Utah. J. Struct. Geol. 20, 3–19. https://doi.org/10.1016/S0191-8141(97)00079-5.
Chang, H.K., Kowsmann, R.O., Figueiredo, A.M.F., Bender, A.A., 1992. Tectonics and stratigraphy of the east Brazil rift system - an overview. Tectonophysics 213, 97–138. https://doi.org/10.1016/B978-0-444-89912-5.50032-6.
Childs, C., Holdsworth, R.E., Jackson, C.A.-L., Manzocchi, T., Walsh, J.J., Yielding, G., 2017. Introduction to the geometry and growth of normal faults. Geol. Soc. Lond. Spec. Publ. 439, 1–9. https://doi.org/10.1144/SP439.24.
Childs, C., Nicol, A., Walsh, J.J., Watterson, J., 2003. The growth and propagation of synsedimentary faults. J. Struct. Geol. 25, 633–648. https://doi.org/10.1016/S0191-8141(02)00054-8.
Cobbold, P.R., Meisling, K.E., Mount, V.S., 2001. Reactivation of an obliquely rifted margin, Campos and Santos basins, southeastern Brazil. AAPG Bull. 85, 1925–1944. https://doi.org/10.1306/8626D0A9-173B-11D7-8645000102C1865D.
Cowie, P.A., Scholz, C.H., 1992. Displacement-length scaling relationship for faults: data synthesis and discussion. J. Struct. Geol. 14, 1149–1156. https://doi.org/10.1016/0191-8141(92)90066-6.
Cox, S., Knackstedt, M., Braun, J., 2001. Principles of Structural Control on Permeability and Fluid Flow in Hydrothermal Systems. https://doi.org/10.5382/rev.14.01.
Davison, I., 1987. Normal fault geometry related to sediment compaction and burial. J. Struct. Geol. 9, 393–401. https://doi.org/10.1016/0191-8141(87)90116-7.
Davison, I., 2007. Geology and Tectonics of the South Atlantic Brazilian Salt Basins, vol. 272. Geological Society, London, Special Publications, p. 15. https://doi.org/10.1144/GSL.SP.2007.272.01.18.
Davison, I., 2009. Faulting and fluid flow through salt. J. Geol. Soc. 166, 205–216. https://doi.org/10.1144/0016-76492008-064.
Davison, I., Anderson, L., Nuttall, P., 2012. Salt deposition, loading and gravity drainage in the Campos and Santos salt basins. Geol. Soc. Lond. Spec. Publ. 363, 159–174. https://doi.org/10.1144/SP363.8.
Demercian, S., Szatmari, P., Cobbold, P., 1993. Style and pattern of salt diapirs due to thin-skinned gravitational gliding, Campos and Santos basins, offshore Brazil. Tectonophysics 228, 393–433. https://doi.org/10.1016/0040-1951(93)90351-J.
Diegel, F.A., Karlo, J., Schuster, D., Shoup, R., Tauvers, P., 1995. Cenozoic Structural Evolution and Tectono-Stratigraphic Framework of the Northern Gulf Coast Continental Margin. https://doi.org/10.1306/m65604c6.
Dow, W.G., 1984. Oil Source Beds and Oil Prospect Definition in the Upper Tertiary of the Gulf Coast. https://doi.org/10.1306/ad4617d2-16f7-11d7-8645000102c1865d.
Dula JR., W.F., 1991. Geometric models of listric normal faults and rollover folds. AAPG Bull. 75, 1609–1625. https://doi.org/10.1306/0C9B29B1-1710-11D7-8645000102C1865D.
Elger, J., Berndt, C., Rüpke, L., Krastel, S., Gross, F., Geissler, W.H., 2018. Submarine slope failures due to pipe structure formation. Nat. Commun. 9, 1–6. https://doi.org/10.1038/s41467-018-03176-1.
Fiduk, J.C., Brush, E.R., Anderson, L.E., Gibbs, P.B., Rowan, M.G., 2004. Salt deformation, magmatism, and hydrocarbon prospectivity in the Espirito Santo Basin, offshore Brazil. https://doi.org/10.5724/gcs.04.24.0640.
Fisher, Q., Knipe, R., 2001. The permeability of faults within siliciclastic petroleum reservoirs of the North Sea and Norwegian Continental Shelf. Mar. Petrol. Geol. 18, 1063–1081. https://doi.org/10.1016/S0264-8172(01)00042-3.
Gamboa, D., Alves, T., Cartwright, J., Terrinha, P., 2010. MTD distribution on a 'passive' continental margin: the Espirito Santo Basin (SE Brazil) during the Palaeogene. Mar. Petrol. Geol. 27, 1311–1324. https://doi.org/10.1016/j.marpetgeo.2010.05.008.
Gamboa, D., Alves, T.M., Cartwright, J., 2012. A submarine channel confluence classification for topographically confined slopes. Mar. Petrol. Geol. 35, 176–189. https://doi.org/10.1016/j.marpetgeo.2012.02.011.
Gamboa, D.A., 2011. An Integrated Seismic-Scale Analysis of Reservoir Compartmentalisation on Continental Margins: the Espirito Santo Basin, SE Brazil. Cardiff University.
Gartrell, A., Zhang, Y., Lisk, M., Dewhurst, D., 2004. Fault intersections as critical hydrocarbon leakage zones: integrated field study and numerical modelling of an example from the Timor Sea, Australia. Mar. Petrol. Geol. 21, 1165–1179. https://doi.org/10.1016/j.marpetgeo.2004.08.001.
Gibbs, P.B., Brush, E.R., Fiduk, J.C., 2003. The evolution of the syn rift and transition phases of the central/southern Brazilian and W. African conjugate margins: the implications for source rock distribution in time and space, and their recognition on seismic data. In: 8th International Congress of the Brazilian Geophysical Society. https://doi.org/10.3997/2214-4609-pdb.168.arq_433.
Hillis, R.R., 2003. Pore pressure/stress coupling and its implications for rock failure. Geol. Soc. Lond. Spec. Publ. 216, 359–368. https://doi.org/10.1144/GSL.SP.2003.216.01.23.
Hovland, M., 2007. Discovery of prolific natural methane seeps at Gullfaks, northern North Sea. Geo Mar. Lett. 27, 197–201. https://doi.org/10.1007/s00367-007-0070-6.
Imber, J., Childs, C., Nell, P.A.R., Walsh, J.J., Hodgetts, D., Flint, S., 2003. Hanging wall fault kinematics and footwall collapse in listric growth fault systems. J. Struct. Geol. 25, 197–208. https://doi.org/10.1016/S0191-8141(02)00034-2.
Jackson, M.P., Hudec, M.R., 2017. Salt Tectonics: Principles and Practice. Cambridge University Press.
Jackson, M.P., Talbot, C.J., 1986. External shapes, strain rates, and dynamics of salt structures. Geol. Soc. Am. Bull. 97, 305–323.
Kim, Y.S., Sanderson, D.J., 2005. The relationship between displacement and length of faults: a review. Earth Sci. Rev. 68, 317–334. https://doi.org/10.1016/j.earscirev.2004.06.003.
Koledoye, B.A., Aydin, A., May, E., 2003. A new process-based methodology for analysis of shale smear along normal faults in the Niger Delta. AAPG Bull. 87, 445–463. https://doi.org/10.1306/08010200131.
Lisle, R.J., Srivastava, D.C., 2004. Test of the frictional reactivation theory for faults and validity of fault-slip analysis. Geology 32, 569–572. https://doi.org/10.1130/G20408.1.
Lopez, J.A., 1990. Structural Styles of Growth Faults in the US Gulf Coast Basin, vol. 50. Geological Society, London, Special Publications, pp. 203–219. https://doi.org/10.1144/gsl.sp.1990.050.01.10.
Mandl, G., 1999. Faulting in Brittle Rocks: an Introduction to the Mechanics of Tectonic Faults. Springer, Berlin.
Mansfield, C., Cartwright, J., 1996. High resolution fault displacement mapping from three-dimensional seismic data: evidence for dip linkage during fault growth. J. Struct. Geol. 18, 249–263. https://doi.org/10.1016/S0191-8141(96)80048-4.
Manzocchi, T., Childs, C., Walsh, J., 2010. Faults and fault properties in hydrocarbon flow models. Geofluids 10, 94–113. https://doi.org/10.1002/9781444394900.ch8.
Mattos, N.H., Alves, T.M., 2018. Corridors of crestal and radial faults linking salt diapirs in the Espirito Santo Basin, SE Brazil. Tectonophysics 728, 55–74. https://doi.org/10.1016/j.tecto.2017.12.025.
Mcneill, L.C., Piper, K.A., Goldfinger, C., Kulm, L.D., Yeats, R.S., 1997. Listric normal faulting on the Cascadia continental margin. J. Geophys. Res. Solid Earth 102, 12123–12138. https://doi.org/10.1029/97JB00728.
Meisling, K.E., Cobbold, P.R., Mount, V.S., 2001. Segmentation of an obliquely rifted margin, Campos and Santos basins, southeastern Brazil. AAPG Bull. 85, 1903–1924. https://doi.org/10.1306/8626d0a9-173b-11d7-8645000102c1865d.
Mello, M., Maxwell, J., 1990. Organic Geochemical and Biological Marker Characterization of Source Rocks and Oils Derived from Lacustrine Environments in the Brazilian Continental Margin. https://doi.org/10.1306/m50523c5 (Chapter 5).
Mohriak, W., Nemčok, M., Enciso, G., 2008. South Atlantic Divergent Margin Evolution: Rift-Border Uplift and Salt Tectonics in the Basins of SE Brazil, vol. 294. Geological Society, London, Special Publications. https://doi.org/10.1144/SP294.19.
Mohriak, W., Rosendahl, B., 2003. Transform zones in the South Atlantic rifted continental margins. Geol. Soc. Lond. Spec. Publ. 210, 211–228. https://doi.org/10.1144/GSL.SP.2003.210.01.13.
Mohriak, W.U., Szatmari, P., Anjos, S., 2012. Salt: geology and tectonics of selected Brazilian basins in their global context 363, 28. https://doi.org/10.1144/SP363.7.
Morris, A., Ferrill, D.A., Henderson, D.B., 1996. Slip-tendency analysis and fault reactivation. Geology 24, 275–278. https://doi.org/10.1130/0091-7613(1996)024%3C0275:STAAFR%3E2.3.CO;2.

Müller, S., Reinhardt, L., Franke, D., Gaedicke, C., Winsemann, J., 2018. Shallow gas accumulations in the German north Sea. Mar. Petrol. Geol. 91, 139–151. https://doi.org/10.1016/J.MARPETGEO.2017.12.016.

Ojeda, H.A.O., 1982. Structural framework, stratigraphy, and evolution of Brazilian marginal basins. AAPG Bullet.-Am. Assoc. Petrol. Geol. 66, 732–749. https://doi.org/10.1306/03B5A309-16D1-11D7-8645000102C1865D.

Peacock, D., Sanderson, D., 1991. Displacements, segment linkage and relay ramps in normal fault zones. J. Struct. Geol. 13, 721–733. https://doi.org/10.1016/0191-8141(91)90033-F.

Piedade, A., Alves, T.M., 2017. Structural styles of Albian rafts in the Espirito Santo Basin (SE Brazil): evidence for late raft compartmentalisation on a 'passive' continental margin. Mar. Petrol. Geol. 79, 201–221. https://doi.org/10.1016/j.marpetgeo.2016.10.023.

Pilcher, R.S., Kilsdonk, B., Trude, J., 2011. Primary basins and their boundaries in the deep-water northern Gulf of Mexico: origin, trap types, and petroleum system implications. AAPG Bull. 95, 219–240. https://doi.org/10.1306/06301010004.

Qin, Y.P., Alves, T.M., Constantine, J., Gamboa, D., 2016. Quantitative seismic geomorphology of a submarine channel system in SE Brazil (Espirito Santo Basin): scale comparison with other submarine channel systems. Mar. Petrol. Geol. 78, 455–473. https://doi.org/10.1016/j.marpetgeo.2016.09.024.

Rouby, D., Guillocheau, F., Robin, C., Bouroullec, R., Raillard, S., Castelltort, S., Nalpas, T., 2003. Rates of deformation of an extensional growth fault/raft system (offshore Congo, West African margin) from combined accommodation measurements and 3-D restoration. Basin Res. 15, 183–200. https://doi.org/10.1046/j.1365-2117.2003.00200.x.

Rowan, M.G., Jackson, M.P.A., Trudgill, B.D., 1999. Salt-related fault families and fault welds in the northern Gulf of Mexico. AAPG Bullet.-Am. Assoc. Petrol. Geol. 83, 1454–1484. https://doi.org/10.23867/ri0268d.

Shelton, J.W., 1984. Listric normal faults - an illustrated summary. AAPG Bullet.-Am. Assoc. Petrol. Geol. 68, 801–815. https://doi.org/10.1306/AD461426-16F7-11D7-8645000102C1865D.

Suppe, J., 2014. Fluid overpressures and strength of the sedimentary upper crust. J. Struct. Geol. 69, 481–492. https://doi.org/10.1016/j.jsg.2014.07.009.

Tao, Z., Alves, T.M., 2019. Impacts of data sampling on the interpretation of normal fault propagation and segment linkage. Tectonophysics 762, 79–96. https://doi.org/10.1016/j.tecto.2019.03.013.

Van Den Berg, A., Weimer, P., Bouroullec, R., 2004. Structural Evolution of the Mensa Minibasin, mississippi Canyon, Northern Deep Gulf of mexico.

Vendeville, B.C., 2005. Salt tectonics driven by sediment progradation: Part I - mechanics and kinematics. AAPG Bull. 89, 1071–1079. https://doi.org/10.1306/03310503063.

Walsh, J.J., Watterson, J., 1988. Analysis of the relationship between displacements and dimensions of faults. J. Struct. Geol. 10, 239–247. https://doi.org/10.1016/0191-8141(88)90057-0.

Watterson, J., 1986. Fault dimensions, displacements and growth. Pure Appl. Geophys. 124, 365–373. https://doi.org/10.1007/BF00875732.

Xiao, H.-B., Suppe, J., 1989. Role of compaction in listric shape of growth normal faults. AAPG Bull. 73, 777–786. https://doi.org/10.1306/44b4a25d-170a-11d7-8645000102c1865d.

Yuan, X.P., Leroy, Y.M., Maillot, B., 2020. Control of fluid pressures on the formation of listric normal faults. Earth Planet Sci. Lett. 529 https://doi.org/10.1016/j.epsl.2019.115849.

Ze, T., Alves, T.M., 2016. The role of gravitational collapse in controlling the evolution of crestal fault systems (Espirito Santo Basin, SE Brazil). J. Struct. Geol. 92, 79–98. https://doi.org/10.1016/j.jsg.2016.09.011.

Ze, T., Alves, T.M., 2021. Localized strata-bound domino faulting offshore Espírito Santo Basin (southeastern Brazil): the case for sudden release of fluid in salt-withdrawal basins. AAPG (Am. Assoc. Pet. Geol.) Bull. 105, 1535–1562. https://doi.org/10.1306/01282117266.